Sustainable Bottom-Up Synthesis of Anisotropic Gold Nanoparticles

By

Patrick Joseph Straney

Bachelor of Science, Chemistry, University of Delaware, 2010

Submitted to the Graduate Faculty of

The Dietrich School of Arts and Science in partial fulfillment

of the requirements for the degree of Masters of Science

University of Pittsburgh

2013

UNIVERSITY OF PITTSBURGH

DIETRICH SCHOOL OF ARTS AND SCIENCES

This thesis was presented

By

Patrick Joseph Straney

It was defended on

April 29th, 2013

and approved by

Nathaniel Rosi, Associate Professor, Department of Chemistry

Geoffrey Hutchison, Assistant Professor, Department of Chemistry

Thesis Advisor: Jill Millstone, Assistant Professor, Department of Chemistry

SUSTAINABLE BOTTOM-UP SYNTHESIS OF ANISOTROPIC GOLD NANOPARTICLES

Patrick J. Straney, M. S.

University of Pittsburgh, 2013

Anisotropic noble metal nanoparticles exhibit unique optical and catalytic properties that have the potential to revolutionize applications ranging from cancer therapy to hydrogen storage. While there is considerable drive for the commercial implementation of these materials, a significant barrier to industrial translation lies in the lack of rational synthetic methods to produce them. This gap introduces difficulties with both the reproducibility and the sustainability of anisotropic nanoparticle synthesis. Here, a robust approach for the solution-phase synthesis of gold nanoparticles of technological interest has been developed. Instead of using a seed template to access canonical gold nanomaterials such as nanorods and nanoprisms, a homogeneous nucleation approach has been developed where nucleation and growth occur in the same chemical environment. By regulating the stages of particle nucleation and growth, nanorods with lengths from 30 to 630 nm and triangular or hexagonal prisms with vertex-to-vertex lengths ranging from 120 to over 700 nm were produced in high yield. These results shed light on the factors that influence the growth of anisotropic nanomaterials, and allow for drastically more efficient synthetic routes. Specifically, this methodology allows for the reduction in the amount of reagents needed to synthesize nanorods and nanoprisms by as much as 90% by weight, and represent the first report of spectroscopically-discernible, colloidal gold nanoplates obtained using a seedless approach. Methods developed will facilitate future investigations concerning the formation of complex, hybrid nanoparticle architectures from anisotropic nanomaterial substrates.

TABLE OF CONTENTS

LIST OF TABLES

LIST OF FIGURES

LIST OF EQUATIONS

ABBREVIATIONS

AgF	Silver Fluoride
$AgNO_3$	Silver Nitrate
CTAB	Cetyltrimethylammonium Bromide
D_2O	Deuterium Oxide
FFT	Fast Fourier Transform
FWHM	Full Width at Half Maximum
$HAuCl_4$	Hydrogen Tetrachloroaurate
HF	Hydrofluoric Acid
HRTEM	High-Resolution Transmission Electron Microscopy
LSPR	Localized Surface Plasmon Resonance
$NaBH_4$	Sodium Borohydride
NaI	Sodium Iodide
NaOH	Sodium Hydroxide
O.D.	Optical Density
rcf	Relative Centrifugal Force
SEM	Scanning Electron Microscopy
SHE	Standard Hydrogen Electrode
SPR	Surface Plasmon Resonance
TEM	Transmission Electron Microscopy
TSK	Terrace-Step-Kink
UPD	Underpotential Deposition
UV-vis-NIR	Ultraviolet-Visible-Near Infrared

1.0 INTRODUCTION

1.1 Anisotropic Noble Metal Nanoparticles

Anisotropic noble metal nanoparticles possess unique physical and chemical properties[1-3] that are dependent upon not only on their composition, but also on their size, shape, and surface chemistry. Over the past two decades, considerable attention has been directed toward developing shape-controlled syntheses of noble metal nanoparticles in order to increase the functionality of these materials[4-6]. In 2001, Murphy et al.[7] revolutionized the field of shape-controlled nanoparticle synthesis by developing a colloidal, seed-mediated synthesis for gold nanorods in high yield. Since the initial discovery of the gold nanorod synthesis, continued efforts focus on expanding the range of synthetically accessible nanoparticle architectures and investigating the properties of such nanomaterials in applications ranging from gene delivery[8, 9] to photovoltaics[10].

1.2 Bottom-Up Synthesis of Anisotropic Nanomaterials

In bottom-up syntheses, colloidal nanoparticle products are formed from the assembly of atomic or molecular constituents, as opposed to top-down methods where products are "carved" from bulk materials. While bottom-up syntheses have clear advantages in terms of throughput and yield, a major downside lies in the ability to control the resulting size, shape, and monodisperisty of products[11]. In part, the inability to control product morphology is due to a lack of mechanistic insight into the processes that govern nanocrystal nucleation and growth[12].

1.3 Nucleation and the LaMer Diagram

The processes of nanoparticle nucleation and growth have been modeled by LaMer and coworkers[13] who investigated the formation of monodisperse hydrosol colloids. Here, nucleation and growth were viewed as a function of the growth monomer concentration in solution over the duration of the reaction (Figure 1.1). As the concentration of the monomer approaches the critical limiting supersaturation point, the total energy of the system can be lowered by the homogeneous nucleation of a solid phase, partially relieving the supersaturation condition. The free energy (ΔG) cost of forming a spherical cluster with radius *r* is modeled with the following equation[14]:

$$\Delta G = \frac{4}{3}\pi r^3 \Delta G_v + 4\pi r^2 \sigma$$

Equation 1.1. Free energy required for homogeneous nucleation[14]

Here, the free energy per unit volume (ΔG_v), accounts for the favorability of a phase transformation due to the supersaturation condition and becomes increasingly negative as the system approaches the critical limiting supersaturation (*Region II).* The driving force for nucleation, however, is counterbalanced by the unfavorable energetic cost of introducing a new solid phase due to surface tension (σ) at the interface. Only under superstation conditions will the formation of a new phase be energetically favorable enough to overcome this energetic barrier imparted by surface tension.

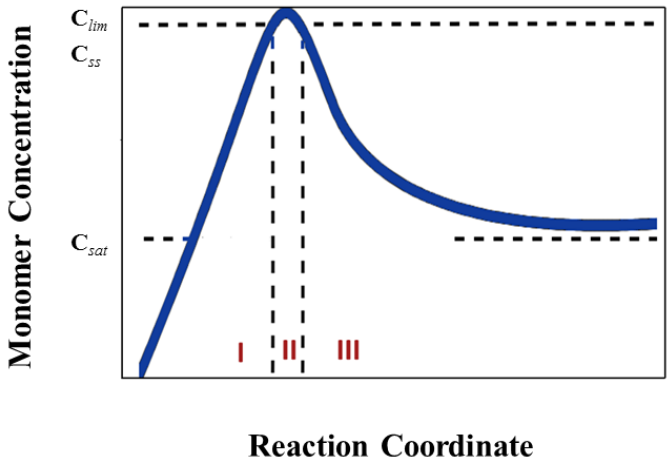

Figure 1.1. The LaMer model of nucleation and growth[13], which depicts the reaction coordinate in terms of increasing monomer concentration. The nucleation of a solid phase occurs when the monomer concentration increases past the supersaturation point (*Css, Region I*) and approaches the critical limiting supersaturation value (C_{lim}, *Region II*). Nucleation continues until the supersaturation condition is relieved, after which particles continue to grow by heterogeneous deposition (*Region III*) until the monomer concentration returns to the saturation point (C_{sat}).

After nucleation of the solid phase, the supersaturation condition is partially relieved, and clusters continue to grow by diffusion of monomer to the solid surface modeled by a process of heterogeneous nucleation, a surface assisted type of nucleation[13]. Here, intermolecular interactions (e.g. adhesive forces) between the solid and liquid phases promote wetting of the solid surface, hence lowering the overall surface tension and the energetic barrier to nucleation[15]. As shown in Equation 1.2,

$$\Delta G_{heterogeneous} = \Delta G_{homogeneous} * \left(\frac{1}{2} - \frac{3}{4}\cos\theta + cos^3\theta\right)$$

Equation 1.2. Free energy required for heterogeneous deposition

heterogeneous nucleation requires less total energy than homogeneous nucleation when there are favorable interactions between the two phases. The strength of the adhesive interactions can be measured by the contact angle (θ) formed at the phase interface (Figure 1.2)[15]. Due to the wetting of the solid surface, heterogeneous nucleation will continue until the system returns to the monomer saturation point (Figure 1.1, *Region III).*

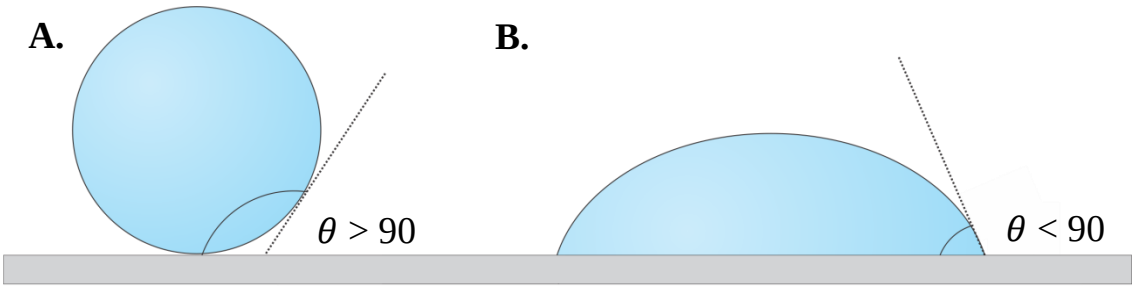

Figure 1.2. The contact angle formed at the phase interface is determined by the strength of the adhesive interactions between phases. At contact angles greater than 90° (A), the adhesive forces formed at the phase interface are not enough to overcome the cohesive forces between solvent molecules, indicating hydrophobicity. Contact angles less than 90°, however, suggest an attractive interaction between the two phases (B).

1.3.1 Terrace-Step-Kink Model of Heterogeneous Nucleation

The terrace-step-kink (TSK) model of adatom deposition onto a stepped crystalline surface is a useful mechanism for describing the growth of nanocrystals via heterogeneous nucleation[16]. Depending on the chemical potential of the nucleation site, an adatom will either be incorporated into the crystalline lattice, or it may dissolve back into solution[17]. The energy required to remove an adatom from a surface is site-dependent and increases with increasing site coordination number. In terms of nanocrystal growth, the TSK model implies that the structure of the crystalline surface will directly impact the rate of atom incorporation depending on the relative proportions of terrace, step, and kink sites on the particle surface. Furthermore, depending on factors such as internal lattice strain or the presence of surface bound adsorbates such as halides or capping ligands, atom incorporation may be impacted further[18]. Slight differences in crystal facet energetics (as related to crystal facet bulk coordination number) have a profound impact on the nanocrystal growth pathway and the resulting nanoparticle morphology[12]. This relationship between nanoparticle surface structure and the probability of adatom incorporation is commonly related to crystal facet poisoning by ligands, and together these effects have become fundamental tenants of shape control on the nanoscale[19]. As shown in Figure 1.3, of the three possible sites on a given surface (terrace, step, or kink), the kink site exhibits the lowest coordination number, and therefore an adsorbing atom would have a higher chance for incorporation within the crystal lattice at that position[20].

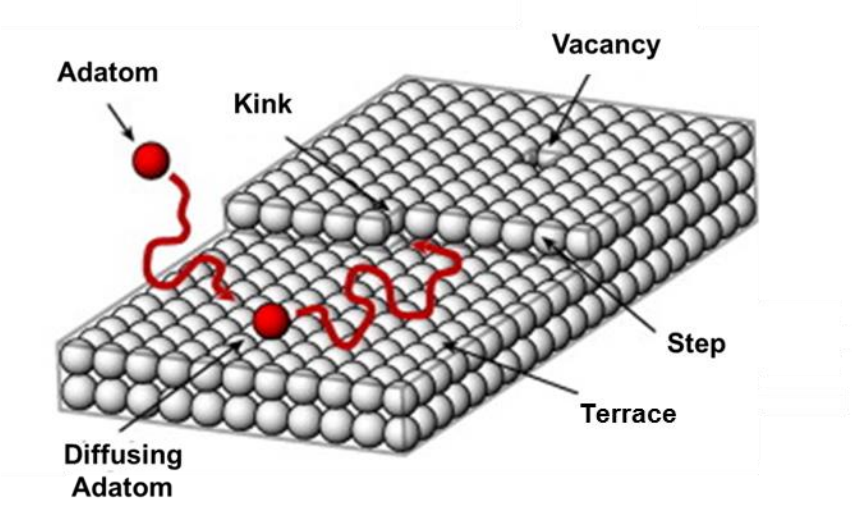

Figure 1.3. According to the terrace-step-kink model, an incoming atom will the opportunity to form more bonds to the surface when adsorbed at a kink site as compared to a step or terrace site, and therefore will have a higher probability of incorporation into the crystalline lattice (reproduced from Reference 20).

1.3.2 Heterogeneous Nucleation and Seed-Mediated Syntheses

As described in the LaMer model of nucleation and growth, homogeneous nucleation will occur until relief of the supersaturation conditions to some extent that is system dependent (Figure 1.1, *Region III*). As soon as a cluster reaches a stable size, it will continue to grow via the described adatom adsorption model. Clusters nucleated early in the reaction coordinate will therefore undergo a longer duration of growth, resulting in polydispersity in nanoparticle size and shape[21]. To avoid heterogeneities in nanoparticle morphology, nucleation and growth are commonly separated in time and chemical environment in a

process referred to as seed-mediated nucleation[22] (Figure 1.4). Here, nucleation sites are created in one chemical environment, where use of a strong reducing agent allows for a brief period of nucleation and less chance of resulting heterogeneity. After formation, these nucleation sites or "seeds" can be introduced to a chemical environment termed a "growth solution" tailored for diffusion-limited, anisotropic growth[22]. Here, both the crystallinity of the seed template as well as the presence of shape directing additives in the growth solution can influence resulting nanoparticle product distribution[23-26]. For example, gold nanorods are formed by the addition of small, single crystal seeds in the presence of silver nitrate[26], while gold nanoprisms are formed from larger, twinned seeds with the addition of sodium iodide[27].

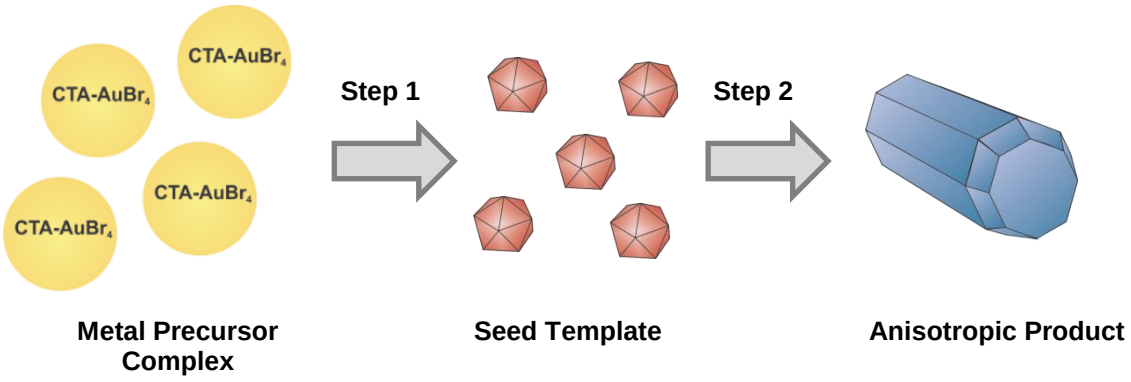

Figure 1.4. Pictorial representation of seed-mediated syntheses in which the nucleation site, the seed template, is first formed by the reduction of metal precursors. In Step 2, the seed will be introduced into a separate chemical environment tailored for anisotropic growth.

1.4 Shape Control in Anisotropic Nanoparticle Synthesis

Currently, shape control on the nanoscale is achieved by the empirical derivation of experimental conditions due to ambiguities in the mechanistic role of the seed in relation to

those of shape directing forces in the growth solution. As indicated by the following discussion on the formation of gold nanorods and nanoprisms, the resulting nanoparticle product morphology is influenced by a variety of shape-directing mechanisms and is therefore difficult to predict a priori.

1.4.1 Nanorod Formation: Silver Underpotential Deposition

In the silver-assisted synthesis of gold nanorods, shape control has been attributed to an underpotential deposition mechanism, where the selective deposition of silver on the Au crystal facets changes the rate of crystal facet growth and hence the resulting product morphology[28, 29]. Underpotential deposition (UPD) is an electrochemical phenomenon where a metallic species in solution can be deposited to form a monolayer on a metallic substrate at a potential less negative than the Nernst potential for the metal[30]. As indicated by Equation 1.3, the potential required for UPD to proceed (ΔE_{UPD}) is dependent upon the difference between the work functions of the substrate (Φ_S) and deposited metal (Φ_M). At a potential equal to ΔE_{UPD}, UPD will proceed to form a monolayer on the substrate, as opposed to bulk deposition which occurs at the equilibrium reduction potential. Alternatively, this deposition process can be viewed as wetting phenomenon, where a less noble metal will spontaneously wet (e.g. deposit) a more noble metallic surface. The reduction potential of the metal precursor, which changes with halide concentration and pH, can alter the UPD process leading to significant changes in the deposition rate or structure of the metal deposits (Figure 1.3)[28, 31]. As a result, UPD has been a useful approach to directing nanocrystal growth.

$$\Delta E_{UPD} = 0.5(\Phi_S - \Phi_M)$$

Equation 1.3. Underpotential Shift

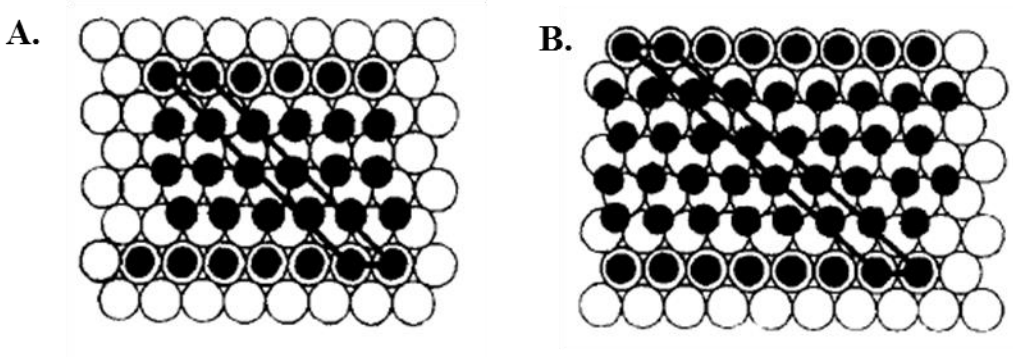

Figure 1.5. Schematics of silver structures deposited on an Au(111) surface in the presence of 0.1 mM HF (A) and 0.5 mM AgF (B) solutions. Here, the small and large circles represent Ag and Au atoms, respectively, while the dark lines indicate the unit cell of the deposit (reproduced from Reference 31).

The UPD mechanism has been commonly been invoked to explain the formation of rod-like architectures in the silver-assisted synthesis of gold nanorods[29, 32]. Here, the selectivity of Ag UPD on Au (110) over that of Au (100) is the driving force for unidirectional growth. As indicated by crystal facet reconstructions[33], the geometric arrangement of the lattice in a (110) facet appears to have a "missing row" of atoms, which creates the regular arrangement of high energy step sites across the crystalline surface. This "missing row" arrangement increases the surface energy of the (110) facet relative to the (100) facet, and therefore increases the rate of Ag UPD. As UPD deposition occurs more quickly on Au (110), the surface is assumed to be covered with a silver monolayer throughout the duration of the reaction. Although the Ag monolayer is eventually oxidized, allowing for continued deposition of Au, overall the UPD process retards or "poisons" growth of the (110) facet.

Conversely, Ag UPD on Au (100) occurs at a slower rate, and therefore the surface remains more accessible for Au deposition throughout the duration of growth. Overall, the net effect of Ag UPD results in elongation primarily in the (100) direction and the formation of rod-shaped nanoparticles.

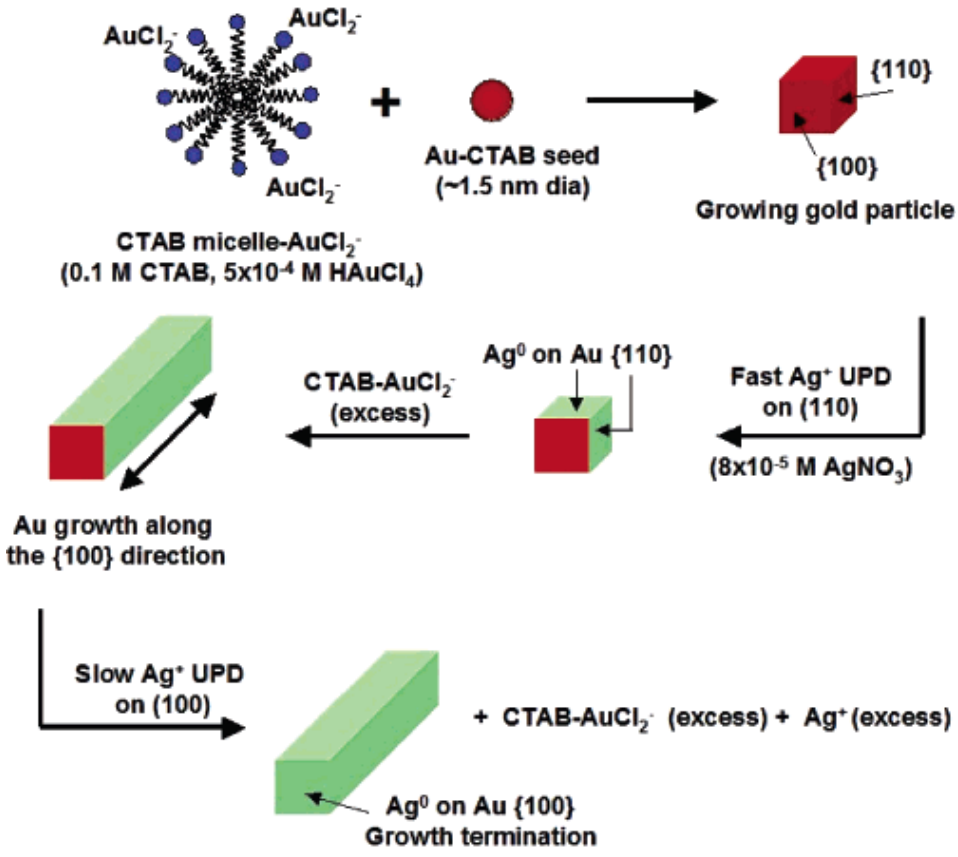

Figure 1.6. Mechanism of silver-assisted gold nanorod formation[29]. Au precursor, bound to the cationic CTAB micelle, will deposit on the (110) and (100) faces of the growing CTAB functionalized Au seed by an underpotential deposition mechanism. Fast UPD of Ag on Au (110) attenuates growth in the [110] direction, yet the (100) facets remains open, promoting

Au deposition in the [100] direction and the formation of rod-like architectures. (Reproduced from Reference 29).

1.4.2 Prism Formation: Factors Influencing 2D Growth

In describing the formation of gold nanoprisms, shape control has been attributed to the presence of twin planes in the crystal lattice in conjunction with crystal facet poisoning of the Au (111) facet by sodium iodide[19, 25]. Nanoprism seeds, formed from the reduction of $HAuCl_4$ by $NaBH_4$ in the presence of trisodium citrate, are 5.2 ± 0.6 nm and consist of a mixture of single crystalline and multiply twinned architectures[24, 27]. As proposed in the silver halide model of plate-like growth[19], such twin planes, which have higher concentration of step and/or kink sites, direct addition to the two adjacent faces of the twin, promoting growth in only two dimensions[34]. Meanwhile, addition to the broad top and bottom faces of the prism is restricted due to the interaction of sodium iodide with the (111) facets of the growing nanocrystal. As confirmed by X-ray photoelectron spectroscopy measurements, iodide interacts more strongly with the top Au (111) facets compared to the side facets[25]. The combined effects of the twin plane and crystal facet poisoning by iodide are thought to drive two-dimensional growth and the formation of plate-like morphologies[25].

1.5 Purification of Nanomaterials

Before further characterization or use of nanoparticle reaction products, separation from reaction byproducts and impurities is required. As the observed chemical and physical properties of nanomaterials can readily change with particle morphology,[35, 36] purification strategies that achieve selectivity based on nanoparticle size and shape are highly desirable. Equally important, nanoparticle products must be separated from excess reagents, reagent

byproducts, and surfactant, which is often difficult to achieve without changes in product morphology or stability[37]. There are a multitude of nanoparticle purification techniques, including but not limited to electrophoresis[38], filtration[39], precipitation by anti-solvent[40], or size exclusion chromatography[41], and centrifugation. Centrifugation is particularly attractive because it is a rapid, inexpensive, and highly reproducible method of achieving size and shape selective purification from reaction impurities.

By varying the speed and duration of the centrifugation process, nanoparticles of desired shape and size can be selectively precipitated out of solution. Here, selectivity is achieved due to the difference in the sedimentation coefficients of nanoparticles of various morphologies (Equation 1.4)[42]. The sedimentation coefficient (S), which accounts for differences in viscosity, molecular weight, and electrostatic interaction of the sedimentating species, is defined as the ratio of a particle's sedimentation velocity (v_t) to the applied acceleration (e.g. centrifugal force, a). For a nanoparticle at a given force, a higher sedimentation coefficient will correspond to a faster sedimentation velocity, hence allowing for selectivity in purification by centrifugation.

$$S = \frac{v_t}{a}$$

Equation 1.4. Sedimentation Coefficient

1.6 Characterization of Nanomaterials

In order to understand the effect of experimental parameters on the resulting nanoparticle morphology or composition, methods to accurately characterize the average dimensions, yields, and spectral features of nanoparticle products are required.

1.6.1 UV-vis-NIR Spectroscopy

Ultraviolet visible near-infrared (UV-vis-NIR) spectroscopy is a useful tool for analyzing the optical properties of a nanoparticle colloidal suspension, and thereby allows for a qualitative approximation of the size and shape distributions of nanoparticle reaction products. Here, assessments concerning nanoparticle size and shape are possible due to an optical phenomenon of noble metal nanoparticles referred to as the localized surface plasmon resonance (LSPR, Figure 1.7).[43] A surface plasmon is the collective oscillation of surface conduction electrons at a dielectric interface caused by incident light. This surface resonance conditions occurs when the frequency of incident light matches that of the electrons on the metallic surface, and therefore changes with nanoparticle morphology[44]. When confined to dimensions of less than 100 nm, the SPR is referred to as a localized surface plasmon (LSPR)[43].

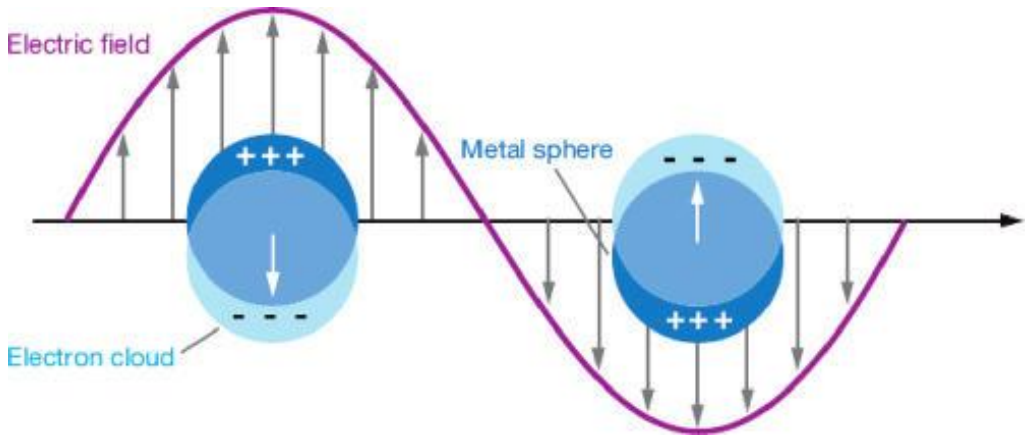

Figure 1.7. Graphical representation of the localized surface plasmon resonance. Electromagnetic radiation incident on the metallic nanoparticle induces the coherent oscillation of surface conduction electrons (reproduced from Reference 43).

Due to this relationship between particle morphology and optical properties, the LSPR excitation wavelength is a useful diagnostic of particle size, shape, and monodisperisty (as indicated by the full width at half maximum of the absorbance peak). As described by the Beer-Lambert (Equation 1.5), the LSPR allows one to determine the concentration (C) of a morphology with a known molar extinction coefficient (ϵ) simply by measuring the absorbance (A) through a given path length (b). It is important to note, however, that the Beer-Lambert law deviates from linearity at high concentrations, the effect of which intensifies with increasing extinction coefficient[45]. Deviations from linearity result at high concentrations of the absorbing species, as decreased intermolecular distances can cause fluctuations in the charge density of the absorbing species, thereby impacting the ability to absorb radiation of a given wavelength. In absorbance determinations for anisotropic noble metals, these deviations become more apparent due to extinction coefficients on the order of 10^9 M^{-1} cm^{-1}.[36] Furthermore, as the extinction coefficient changes with particle morphology[46], it is important to note that Uv-vis-NIR analyses of nanoparticle yield or monodisperisty are strictly qualitative.

$$A = \epsilon b C$$

Equation 1.5. Beer-Lambert Law

1.6.2 Electron Microscopy

Electron microscopy is an invaluable asset in characterizing nanomaterials, as the resolution of this technique allows for direct visualization of nanoscale structural details. To date, resolutions better than 50 pm at magnifications of about 10,000,000x has been achieved using this technique.[47]

1.6.2.1 Transmission Electron Microscopy

In transmission electron microscopy (TEM), a beam of electrons is transmitted through the sample. Depending on the mode of TEM operation, image contrast is achieved by the combination of several different phenomena. For example, in bright field mode (normal operation conditions), contrast is a function of sample thickness, Z-number, and crystallinity as less electrons are transmitted through thicker samples, those with larger nuclei, or with increased crystallinity due to electron scattering by the sample[48]. Furthermore, elements will higher atomic numbers will scatter more electrons, causing fewer electrons to reach the detector and contrast derived from differences in atomic number. In another mode of operation referred to as dark field mode, only scattered electrons are used to generate the observed image. Hence, dark field mode is more useful for elemental analysis as the intensity of scattered electrons directly correlates to atomic number.[11] Other possible analytical techniques involve analyzing inelastically scattered electrons, such as electron-energy loss spectroscopy and energy dispersive X-ray spectroscopy which can provide elemental information about the sample

1.6.2.2 Scanning Electron Microscopy

In scanning electron microscopy (SEM), an image is produced by scanning a surface with an electron beam and imaging the resulting backscattered and secondary electrons with a detector[11]. The electron beam used in SEM may be generated by a field emission source and is focused by a series of condensers to a spot size ranging from 0.4 to 5 nm in diameter. The narrow spot size allows for a large depth of field, which is defined as the distance between the nearest and farthest objects that can appear in focus[49]. Together, the rastering of the

beam across the sample, combined with the large depth of field, provide SEM images with high z-resolution, imparting a 3D quality to sample morphology in SEM images. As a characterization technique, SEM is most commonly used to analyze the surface topography and morphology of the sample and for determining the elemental composition at the surface.

1.7 Sustainable Nanochemistry and the Viability of Nanotechnology

Advancing nanotechnology from the laboratory to the industrial setting will require improved synthetic techniques and purification protocols[50]. For example, anisotropic nanoparticle syntheses are commonly low-yielding and irreproducible. Such detriments arise from a lack of mechanistic understanding and ultimately hinder the advancement of nanotechnology. In order to advance the synthetic efficiency of nanoparticle syntheses, future synthetic development should be guided by the 12 Principles of Sustainable Chemistry[51]. Green chemistry principles begin with three fundamental tenets: prevention of waste, atom economy, and the reduction of hazardous materials.[51] Prevention of waste leads to the elimination of unnecessary reagents from a given synthetic pathway and, from a nanochemistry perspective, also presents the opportunity to eliminate mechanistic "red-herrings." Here, improving atom economy is interpreted for nanochemistry as a more efficient use of reagents in order to maximize product atoms out for reagent atoms in. This efficiency can be particularly challenging for reagents such as surfactants which have concentration dependent supramolecular architectures that may or may not impact final nanoparticle outcomes.[19, 26, 52-55] Finally, a more efficient synthesis in terms of steps, reagent use, and reaction conditions (e. g. temperature and pressure) simultaneously addresses issues of synthetic hazards both up and downstream of the synthetic process.

1.8 Specific Aims

The goal of this project is to thoroughly investigate the role of the seed in seed-mediated syntheses. In doing so, the role of the seed in determining the growth pathways of anisotropic nanomaterials can be further elucidated, thereby highlighting critical factors in the stages of anisotropic nanoparticle growth. With advanced mechanistic insight, sustainable and scalable alternatives to seed-mediated syntheses can be developed.

The specific aims of this project include:

Specific Aim I: Develop mechanistic parameters that contribute to the better understanding of anisotropic noble metal nanoparticle synthesis

Specific Aim II: Use insights gained Specific Aim I to improve reaction scalability and sustainability for the increased prospect of translation into industry

Specific Aim III: Incorporate mechanistic insight with sustainable reaction methodologies to increase the range of synthetically accessible nanomaterial compositions and architectures

2.0 EXPERIMENTAL

2.1 Materials

Cetyltrimethylammonium bromide (CTAB, 99%), hydrogen tetrachloroaurate trihydrate ($HAuCl_4 \cdot 3H_2O$, 99.99%), L-ascorbic acid (99%), potassium hexachloroplatinate(IV) (K_2PtCl_6, >99.99%), silver nitrate ($AgNO_3$, 99.9999%), sodium borohydride ($NaBH_4$, 99.99%), sodium hydroxide (99.99%), sodium iodide (NaI, 99.999%), and trisodium citrate (99%) were obtained from Sigma Aldrich (St. Louis, MO) and used as received. All solutions were prepared using NANOpure™ (Thermo Scientific, 18.2 MΩ · cm) water and were made fresh prior to use. Formvar-coated 400 copper mesh grids for TEM analysis and silicon wafer substrates (p-type, 200 nm thermal oxide (silicon dioxide, SiO_2)) for SEM analysis were purchased from Ted Pella Inc. (Redding, CA). All water used during synthesis and work-up is NANOpure™. All reagents were used in air at room temperature unless otherwise noted. All solutions were prepared in water unless otherwise noted.

2.2 General

2.2.1 Glassware Cleaning Procedure

For the following procedures, all glassware was washed with aqua regia (3:1 hydrochloric acid to nitric acid by volume) and rinsed copiously with water. *Caution: aqua regia is toxic and corrosive and must be handled in a fume hood with proper personal protection equipment.* Glassware was then covered with aluminum foil and dried in an oven at 150 °C

2.2.2 CTAB Solution Preparation

CTAB solutions (at various concentrations) were prepared by heating the sealed mixture in a water bath (37 ºC) until it became clear. The solution was then sonicated for 30 seconds and allowed to cool to room temperature before use. If recrystallization of CTAB occurred either during storage or during use, the solution was treated as described above before continuing with the following reactions.

2.3 Seeded Syntheses

2.3.1 Nanorods

Seed-mediated nanorods were prepared according to the literature procedure[26]. In a typical synthesis, CTAB-functionalized nanorods seeds were prepared by adding 5 mL of 0.2 M CTAB to 5 mL of 1 mM $HAuCl_4$. Next, 0.6 mL of a 10 mM $NaBH_4$ solution (freshly prepared, 0°C) was added to the $HAuCl_4$/CTAB solution while rapidly stirring. After addition of the $NaBH_4$, the solution was allowed to stir for 60 seconds and then aged for two hours to allow for complete degradation of the $NaBH_4$. A nanorod growth solution was prepared by sequentially adding 0.1 mL of 4 mM $AgNO_3$, 5.0 mL of 1 mM $HAuCl_4$ and 0.05 mL of 100 mM L-ascorbic acid to 5.0 mL of 0.2 M CTAB. After briefly stirring the growth solution, 12.0 µL of the CTAB-functionalized seeds were added, the solution was stirred for several seconds, and allowed to rest for two hours until nanorod growth was complete.

2.3.2 Prisms

Seed-mediated prisms were prepared according to literature protocols[25]. In a typical synthesis, citrate-functionalized seeds were first prepared by adding 1.0 mL of 10 mM trisodium citrate and 1.0 mL of 10 mM $HAuCl_4$ to 36 mL of H_2O in a 100 mL round bottom flask with a Teflon coated stir bar. The solution was stirred at 1000 rpm, and 1.0 mL of a

freshly prepared solution of 100 mM $NaBH_4$ was rapidly injected. The solution was allowed to rest for two hours before usage to allow for complete degradation of excess $NaBH_4$. Two portions of growth solution (A, B) were prepared by the sequential addition of 0.25 mL of 10 mM $HAuCl_4$, 0.05 mL of 100 mM NaOH, and 0.05 mL of 100 mM L-ascorbic acid to 9.0 mL of a 50 mM CTAB solution (50 μM in NaI). The reaction mixture was briefly stirred after each addition, and final solution was transparent in color. Lastly, another portion of growth solution (C) was prepared in a similar manner, except that the volume of all reagents was increased by a factor of ten. After preparation of the growth solutions, 1.0 mL of the citrate-functionalized seed solution was added to growth solution A. The solution stirred for two seconds, and 1.0 mL of growth solution A was added to growth solution B. Again, the solution was stirred for two seconds, and the entire mixture was added to growth solution C. The reaction was briefly mixed and allowed to rest for two hours until prism formation was complete.

2.4 Seedless Syntheses

2.4.1 Nanorods

In a typical synthesis, 5 mL of aqueous 200 mM CTAB solution was prepared and added to a 20 mL scintillation vial. To this, 100 μL of 4 mM $AgNO_3$ was added and the solution was mixed gently by shaking. Next, 5 mL of 1 mM $HAuCl_4 \cdot 3H_2O$ was added and the solution was mixed briefly by shaking. Upon addition of 50 μL of 100 mM L-ascorbic acid, the orange solution was stirred until turning colorless. Growth was initiated by injecting 1-100 μL of freshly prepared 2.25 mM $NaBH_4$ while stirring on a benchtop vortex mixer (Analog Vortex Mixer, 120V, 50/60Hz, Fisher Scientific). Mixing was continued for 10 seconds, after which the solution was left undisturbed for 30 minutes.

2.4.2 Prisms

In a typical synthesis, 10 μL of 50 mM NaI was added to 10 mL of 50 mM CTAB. Following preparation of the surfactant-salt mixture, 275 μL of 10 mM $HAuCl_4 \bullet 3H_2O$ was added to the solution, followed by the addition of 55 μL of 100 mM L-ascorbic acid, after which the solution turned from orange to clear. To initiate nanoprism growth, a solution of 25 μM $NaBH_4$ was prepared, and 2.5-8.5 μL was added to the growth solution while slowly mixing on a vortex mixer. Mixing was continued for 10 seconds, and the solution was left undisturbed for 30 minutes. Purification of the reaction mixture was carried out by dividing the solution into 1.5 mL centrifuge tubes, and allowing the nanoplates to separate via sedimentation. Nanoprisms were separated from reaction impurities by removal of the supernatant and were stored in 50 mM CTAB.

N.B. In the absence of NaI, this synthesis results in the formation of pentatwinned nanorods when the ratio of $NaBH_4$ to $HAuCl_4$ is changed from the above range for prism formation to values ranging from 0.045 to 0.18.

2.5 CTAB Efficient Syntheses Concentrated solutions of seedless nanorods and nanoprisms were prepared as described above, except that all stock solutions were increased in concentration while the concentration of CTAB remained unchanged. For example, in a synthesis denoted as a **5x** synthesis, the stock solution concentrations of $HAuCl_4$, $AgNO_3$, ascorbic acid, and $NaBH_4$ were increased by a factor of 5 (to 5 mM, 20 mM, 500 mM, 11.25 mM, respectively) while the concentration of the CTAB solution remained at 200 mM.

2.6 Purification Methods

Nanoparticle products were purified by centrifugation at 70 relative centrifugal force (rcf) for 20 mintues (nanoprisms) or at 6000 RCF for five minutes (nanorods). After removal of the supernatant via syringe, nanoparticle pellets were resuspended in H_2O and the entire process was repeated two additional times.

2.7 Characterization Methods

2.7.1 UV-vis-NIR Spectroscopy

Colloids were diluted to an optical density of less than 1.0 optical density (O.D.) for analysis. In all cases, spectra were collected against a background of pure solvent (H_2O or D_2O). For spectral analysis of the prisms, the prisms were purified by centrifugation and resuspended in a 1 mM CTAB solution in D_2O two times to remove residual H_2O. In syntheses for efficient CTAB usage, colloids were volumetrically diluted to their standard concentration prior to analysis (for example, for a seedless **5x** efficient synthesis, samples were diluted to 20% of the original concentration).

2.7.2 Transmission Electron Microscopy Analysis

A 1 mL aliquot of particles, as synthesized, was centrifuged (Eppendorf Centrifuge 5424, rotor FA-45-24-11; 5424/5424R) at speeds and durations described above. After removal of the supernatant via syringe, particles were resuspended in 1 mL of water. This procedure was performed two additional times, after which particles were again collected by centrifugation and resuspended in 50 μL of water. A 10 μL aliquot of concentrated particles was drop cast onto a Formvar-backed copper TEM grid (Ted Pella, Formvar on 400 mesh Cu) and was slowly dried in a humid environment. Samples were imaged on a FEI Morgagni

268 at 80 kV. TEM images were analyzed using ImageJ (open access software, http://rsbweb.nih.gov/ij/), using the particle analysis feature. Over 100 nanoparticles were measured to obtain reported values. All reported errors are the standard deviation in these measurements.

2.7.3 Scanning Electron Microscopy Analysis

Silicon wafer substrates (University Wafer, p-type, silicon dioxide) were first cleaned by sonicating in ethanol for five minutes. The substrate was then successively rinsed with ethanol and acetone, and dried under a stream of N_2 (*g*). Samples were prepared using the same procedure described for TEM analysis. Here, 10 μL of the resulting solution was drop cast onto the wafer and allowed to dry before imaging on a Raith Dual Beam EBL-SEM at various accelerating voltages.

2.7.4 pH Determination

After addition of ascorbic acid, the pH of the growth solutions for seeded and seedless protocols was measured with a 8172BNWP ROSS Sure-Flow Combination electrode (Thermo Scientific), and Orion 3 Star pH benchtop meter, calibrated with buffered solutions at pH 4, 7, and 10 (Fischer Scientific).

3.0 RESULTS AND DISCUSSION

3.1 Time Dependence of Templating Efficiency by Seed

Seed-mediated syntheses exhibit time dependent changes in templating efficiency which ultimately detract from the reproducibility and utility of such approaches. Here, templating efficiency is defined as the ability of a seed population to form a single anisotropic morphology, such as a nanorod, without observable heterogeneities in product size and shape. As the structure of a seed is dynamic in solution, as after formation seeds undergo processes such as Ostwald ripening and coalescence which can change the size, shape, and/or crystallinity of the seed over time[56]. As a result, the seed reagent has a limited active lifetime for templating anisotropic growth. For example, the age of the seed reagent contributes product heterogeneity in these syntheses, where the aspect ratio of seed-mediated nanorods decreases with increasing seed age.

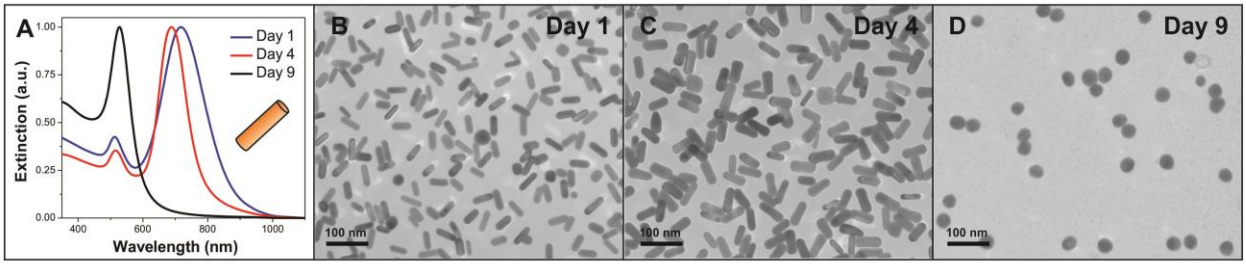

Figure 3.1. UV-vis-NIR extinction spectra (A) and transmission electron microscopy images (B-D) of nanoparticles produced using seeds of varying age. In all cases, the same batch of nanoparticle seeds was used to initiate particle growth. Seeds were stored at room temperature in a sealed glass vial and protected from light. After one day of aging, seeds produced rods in high yield (B). After four days of aging, a blue-shift is observed in the

longitudinal LSPR (A,C). After nine days of aging, the seeds no longer produce anisotropic products (D). Average aspect ratios of particles for days 1, 4, and 9 were 2.6 ± 0.5, 2.2 ± 0.7, and 1.1 ± 0.2, respectively.

3.2 Homogeneous Nucleation Pathway to Anisotropic Nanomaterials

Using reaction conditions similar to those detailed in the seed-mediated synthetic protocols for gold nanorods[26] and nanoprisms[25], a seedless protocol was developed. In order to further understand the nanoparticle nucleation and growth in the absence of a seed template, synthetic products of the seed-mediated and seedless syntheses were compared using SEM, TEM, and UV-vis-NIR spectrophotometry (Figure 3.2).

Without the separation of nucleation and growth in time and chemical environment, multiple nucleation events throughout the duration of the reaction could lead to polydispersity in nanoparticle size and shape. Therefore, a strong reducing agent, sodium borohydride (reduction potential of -1.24 eV vs standard hydrogen electrode (SHE))[57], was selected, as it quickly degrades ($t_{1/2}$ = 0.0607 minutes at pH = 7).[58] The rapid reduction of the gold precursor briefly increases the concentration of the gold monomer over the critical supersaturation limit required for nucleation. In doing so, a short burst of nucleation was achieved, followed by monodisperse, diffusion-limited growth in the same chemical environment. As shown by previous work independently reported by El-Sayed et al.[6] and Catherine J. Murphy[7], it is clear that final nanoparticle shape is influenced by the rate of gold precursor reduction due to changes in the concentration of gold monomer available for growth. Therefore, it was reasoned that by adjusting the ratio of $NaBH_4$:$HAuCl_4$, shape-controlled, monodisperse growth could be attained.

Tuning the ratio of $NaBH_4$:$HAuCl_4$ in the presence of silver nitrate or sodium iodide allowed for the formation of gold nanorods and nanoprisms, respectively. Nanorods were produced in greater than 90% yield and prisms in approximately 60% yield, comparable to as-synthesized yields reported using seed-mediated protocols[26, 59] Nanorods (length = 40 ± 5 nm, diameter = 16 ± 4 nm, Figure 3.2 A), were produced in comparable yield (> 90%) but with improved monodisperisty, as indicated by the full width at half-max (FWHM, Figure 3.2 C). Purified nanorods and nanoprisms synthesized via seedless initiation were also comparable in size, shape and monodispersity to products obtained using seed-mediated approaches (Figure 3.2). UV-vis-NIR extinction spectra of nanorods produced using seedless initiation exhibited a characteristic longitudinal LSPR at 790 nm and a transverse LSPR at 512 nm (Figure 3.2 C), in agreement with previous studies on $NaBH_4$ mediated growth of gold nanorods.[60] Nanoprisms (edge length = 186 ± 16 nm, thickness = 9 ± 1 nm) exhibited an in-plane dipole band at ~1400 nm and a quadrupole band at ~850 nm, consistent with previous literature reports (Figure 3.2 B, D).[35, 59]

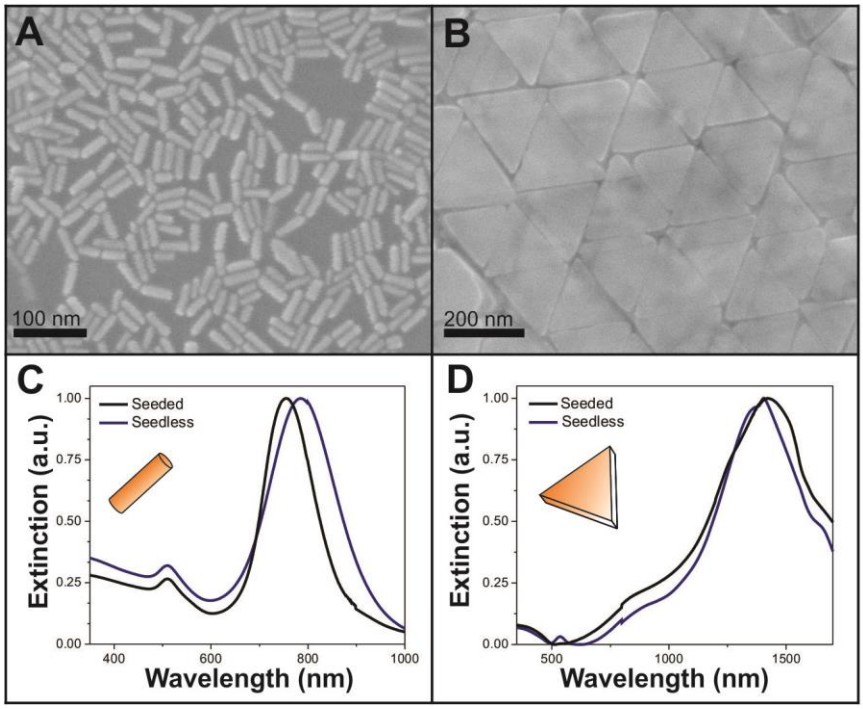

Figure 3.2. SEM images of nanorods (A) and nanoprisms (B) synthesized via seedless initiation, and corresponding UV-vis-NIR spectra (C, D) showing characteristic optical features.

3.3 Shape Control in the Seedless Syntheses

3.3.1 Tuning the Morphology of Seedless Nanorods

As observed in the seeded synthesis, by changing the concentration of silver nitrate in the growth solution, the location of the longitudinal LSPR could be tuned from 650 to 810 nm Figure 3.3). Here, the change in rod length with silver concentration is a kinetic effect; by adding more silver, the Au (110) face is less accessible for growth (see Section 1.4.1), causing an increase in the average length of the rods from 30 to 55 nm.[29]

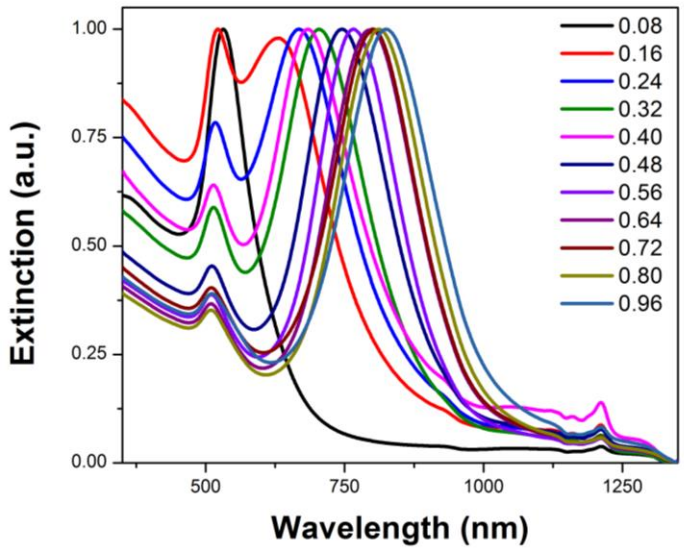

Figure 3.3. UV-vis-NIR extinction spectra of Au nanorods synthesized using a seedless method indicating the systematic increase in nanorod aspect ratio as a function of $AgNO_3$ concentration, as previously reported by El-Sayed et al.[26]

At a given concentration of silver nitrate, the morphology of the rod can be further tuned by adjusting the $NaBH_4$:$HAuCl_4$ ratio (Figure 3.4). Here, the amount of gold consumed during the nucleation event can be modulated, thereby directly influencing the amount of gold remaining for nanorod growth. Ratios of $NaBH_4$:$HAuCl_4$ found to produce rod like growth were from 0.00045 to 0.045. At lower ratios, excess gold remained after growth, as indicated by the decreased rod yield and increased absorbance in the UV regime (Figure 3.4 A). At higher ratios of $NaBH_4$:$HAuCl_4$, growth became progressively isotropic, as an insufficient amount of gold led to a shortened duration of the growth phase.

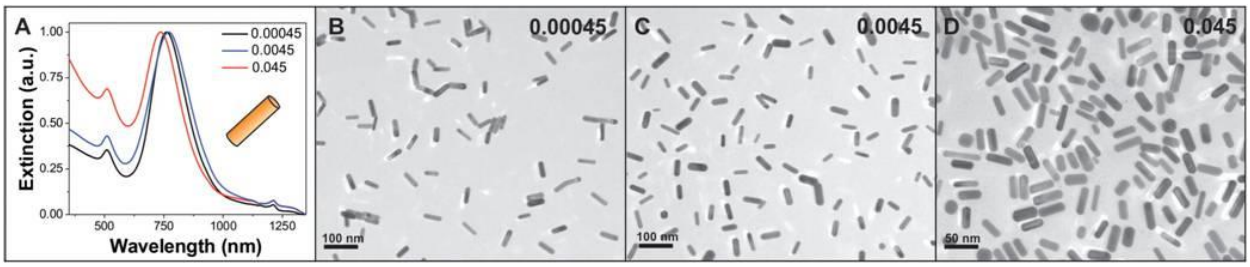

Figure 3.4. UV-vis-NIR spectra (A) and corresponding TEM images of nanorods produced over a range of $NaBH_4$:$HAuCl_4$ concentration ratios (B-D). At low reducing agent to metal precursor ratios (0.00045) (B), nanorods exhibit average lengths of 51 ± 4 nm with a corresponding LSPR at 770 nm. As the ratio of $NaBH_4$:$HAuCl_4$ is increased, nanorod length decreases (47 ± 5 nm, 35 ± 5 nm) and λ_{max} blueshifts (762 nm, 735 nm) at ratios of 0.0045 (C) and 0.045 (D), respectively.

At higher ratios of reducing agent to metal precursor (≥ 0.045), a significant population of pseudospherical particles was observed along with a decreased yield of nanorods (Figure 3.5). Here, the increase in pseudo-spherical particles may be attributed to an excess of nucleation sites in solution produced by the high concentration of reducing agent. When more gold is consumed during the nucleation event, the subsequent phase of particle growth by diffusion is effectively shorter, where the concentration of free gold is depleted before rod-like architectures emerge in high yield.

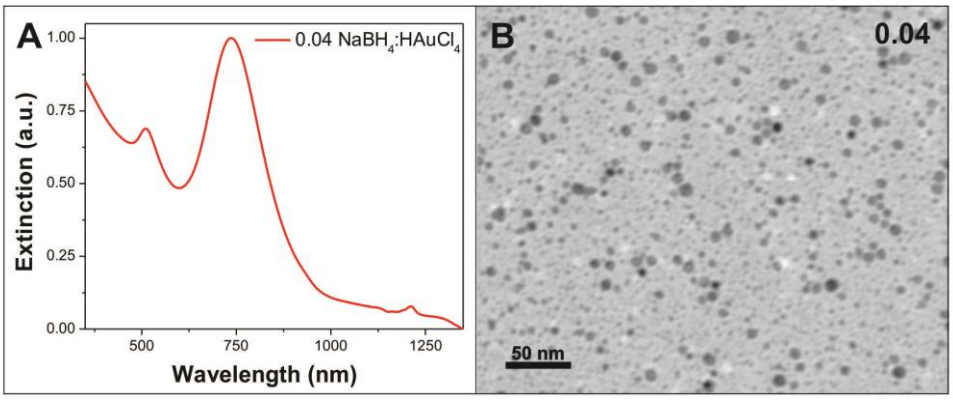

Figure 3.5. UV-vis-NIR spectrum (A) and selected TEM image (B) of nanoparticles produced in nanorod syntheses using higher reducing agent to metal precursor ratios (e. g. 0.045, $NaBH_4$:$HAuCl_4$) examined for the nanorod synthesis. Here, in addition to nanorods, a significant population of pseudo-spherical impurities was observed (representative particles are shown in panel B). The increase in pseudo-spherical NPs may be attributed to an "excess" of nucleation sites in solution produced by the high concentration of reducing agent. With more gold consumed during nucleation, the subsequent phase of particle growth by diffusion is effectively shorter, where the concentration of free gold is depleted before rod-like architectures emerge in high yield. This explanation is consistent with the recently proposed stochastic formation mechanism[61], where nuclei remain dormant until an activation event, and then proceed to grow rapidly after activation. If the available gold precursor is exhausted prior to this activation event, pseudo-spherical impurities subsist.

3.3.2 Tuning the Morphology of Seedless Nanoprisms

The edge length and shape of seedless nanoprisms was found to change with the ratio of $NaBH_4$:$HAuCl_4$. Similarly to the seedless nanorod synthesis, comparable trends in product shape and spectral features were observed, where ratios of 0.0225 to 0.1 produced the desired

shape in comparable yield to the analogous seed-mediated procedure (Figure 3.6). However, the range of $NaBH_4$:$HAuCl_4$ ratios that resulted in plate-like growth was found to be more narrow than for the seedless nanorod synthesis, and changes in product morphology were more pronounced. At a $NaBH_4$:$HAuCl_4$ ratio of 0.1, the major product was triangular nanoprisms (yield ~60%). At the lowest concentration of $NaBH_4$ found to promote plate-like growth (0.025), the nanoplates became hexagonal in shape with an average vertex-to-vertex length of 720 ± 70 nm. Although the particle shape recovers symmetry, the dipole LSPR shifts from 1420 to over 1600 nm and there is a marked broadening of the peak, likely due to particle scattering[35]. At ratios greater than 0.1, a marked increase in isotropic growth was observed, and the yield of nanoprisms decreased.

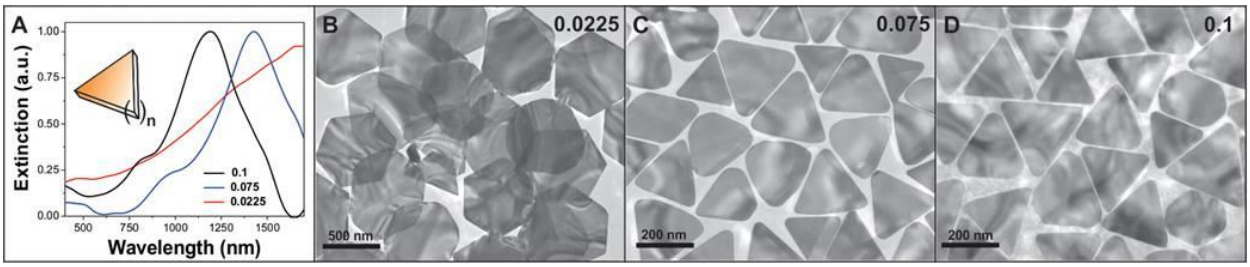

Figure 3.6. UV-vis-NIR spectra (A) and corresponding TEM images of nanoprisms produced over a range of $NaBH_4$:$HAuCl_4$ concentration ratios (B-D). At the lowest concentration of reducing agent relative to gold precursor (0.0225) (B), prisms exhibit hexagonal morphologies with an average vertex-to-vertex distance of 720 ± 20 nm and a corresponding in-plane dipole LSPR at 1674 nm. As the ratio of reducing agent to metal precursor increases, nanoprisms become triangular in shape with decreasing edge lengths (153 ± 21 nm, 120 ± 18 nm) and blue-shifted λ_{max} (1420 nm, 1180 nm) at ratios of 0.075 (C) and 0.1 (D), respectively.

3.3.3 Tuning the Morphology of Pentatwinned Rods

In addition to the silver-assisted gold nanorods and nanoprisms, pentatwinned nanorods were also synthesized using a seedless initiation approach. Due to the five-fold symmetry of pentatwinned rods, it has been postulated these a pentagonally twinned seed is necessary for rod formation[19, 24]. Surprisingly, however, pentatwinned rods could be formed in high yield without use of a seed template (Figure 3.7). As in the previous examples with silver-assisted nanorods and nanoprisms, the ratio of $NaBH_4$ to $HAuCl_4$ was found to have an influence on the nanoparticle morphology, with ranges of 0.045 to 0.18 producing rods of average lengths ranging from 630 to 460 nm, respectively. Again, this is evidence that crystallographic features such as twin planes develop during growth regardless of the nucleation conditions and are not shape directing attributes of the seed template

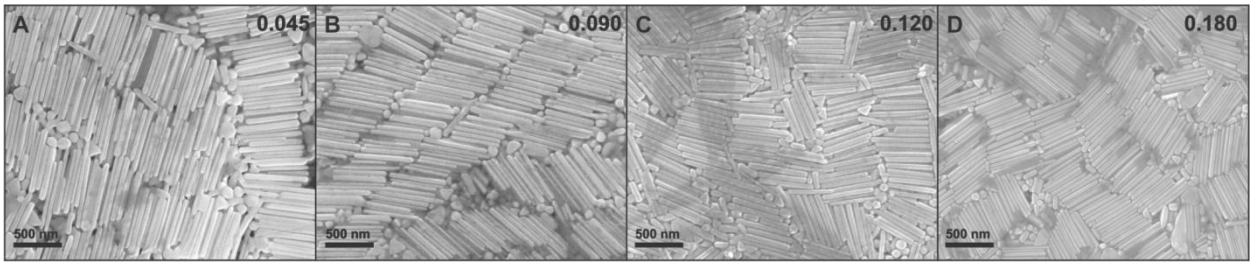

Figure 3.7. SEM of penta-twinned high aspect ratio gold nanorods synthesized using a seedless method based on the silver-less synthesis developed by Murphy et al. At the lowest ratio of NaBH4:HAuCl4 (A, 0.045), rods were 631 ± 64 nm in length by 27 ± 7 nm wide. As the amount of reducing agent increased relative to gold precursor, the length of the rods decreased (575 ± 70 nm, 498 ± 36 nm, and 459 ± 32 nm for B, C, and D, respectively. The widths of the rods were measured to be 27 ± 8, 41 ± 11, 40 ± 10, and 39 ± 10 for A, B, C, and D, respectively.

3.4 HRTEM Comparison of Seed-Mediated and Seedless Product Crystallinity

The crystallinity of products obtained via seedless initiation match their counterparts formed using seed-mediated protocols (Figure 3.8). Fast Fourier transform (FFT) analysis of high resolution transmission electron microscopy (HRTEM) images of nanorods aligned with the [011] zone axis is consistent with previous literature reports.[62] Similarly, nanoprisms demonstrate similar crystalline architectures regardless of the method of initiation. In conclusion, it seems that the crystallinity of the resulting nanoparticle does not depend on the method used to generate the nanoparticle nuclei. Instead, the similarity of products formed using two routes suggests that the anisotropic growth of colloidal gold nanoparticles may be most strongly influenced by the presence of shape directing additives (e.g. metal salts or halides) rather than the nucleation pathway

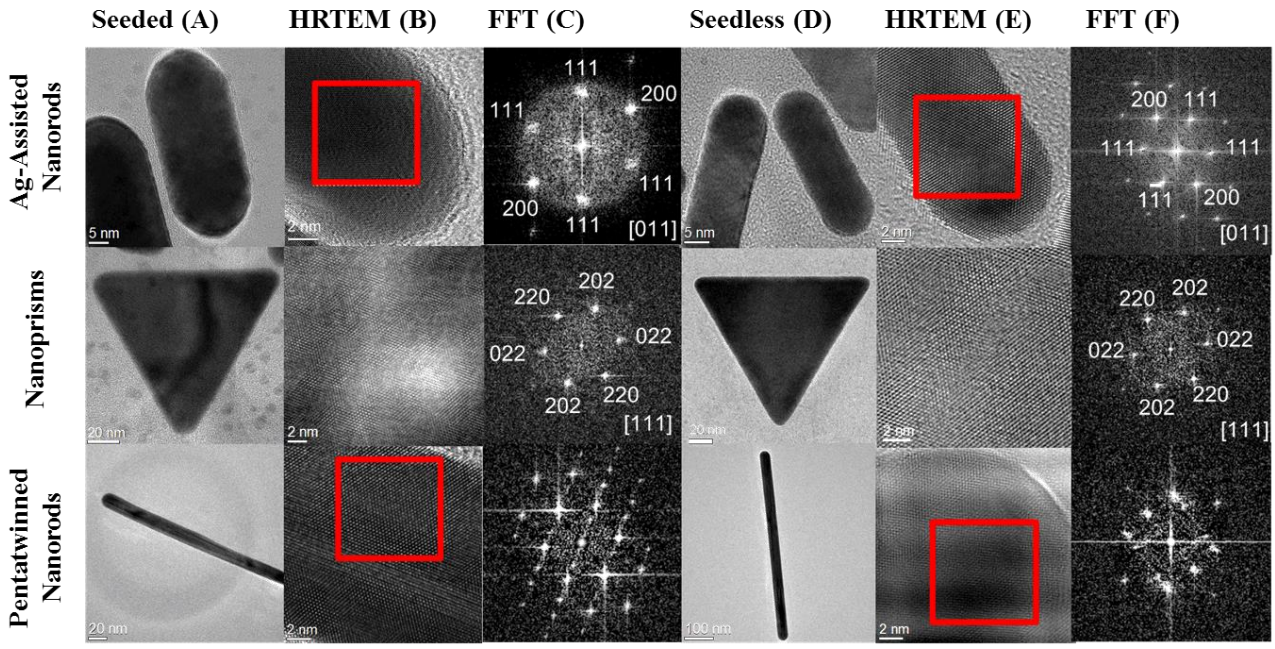

Figure 3.8. HRTEM analysis of particle morphology (A,D,), lattice planes (B,E) and FFT analysis (C,F) of the lattice plane spacing for anisotropic nanoparticles produced using seeded and seedless methods, respectively.

3.5 Reevaluating Surfactant Usage

As CTAB has been shown to be both cytotoxic[63] and difficult to purify[26], developing conditions for efficient CTAB usage is critical for the viability of nanoparticle synthesis and applications. Furthermore, because CTAB is present in near-molar concentrations, it also dominates the synthetic cost of anisotropic gold nanoparticles — more than 4-6 times the cost of the constituent gold.

3.5.1 Reduction in Surfactant Concentration Promotes Isotropic Growth

Above the critical micelle concentration of, CTAB can form supramolecular architectures in solution which may or may not have an impact of the final nanoparticle morphology.[26, 52-55] As expected, attempts to directly reduce the surfactant concentration in these syntheses led to increased particle heterogeneity and increasingly isotropic growth. As indicated in Figure 3.9, nanorods were produced at standard surfactant concentrations of surfactant in 95% yield with lengths of 47 ± 5 nm. Upon a 50% decrease in the surfactant concentration (to 50 mM), the average rod length decreased to 39 ± 4 nm. A further 50% decrease (to 25 mM) caused no further changes in rod length, however, the yield of nanorods compared to pseudo-spherical products was reduced from 95% to 71%.

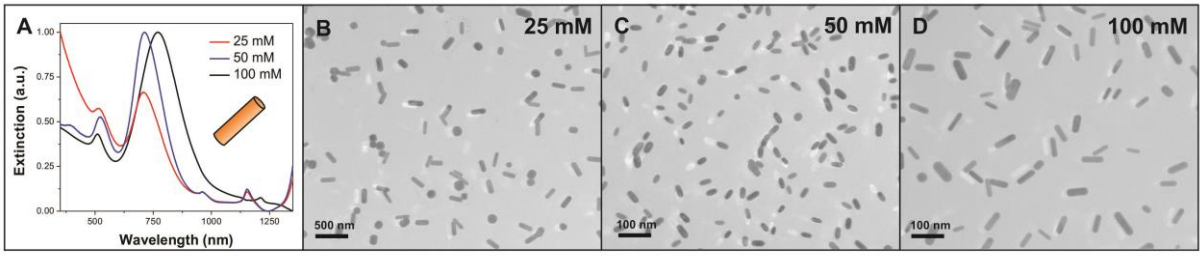

Figure 3.9. UV-vis-NIR extinction spectra (A) and transmission electron microscopy images (B-D) of nanoparticles produced using different CTAB concentrations. In a typical nanorod synthesis, as the concentration of CTAB increases, the yield of nanorods increases. At standard reaction concentrations, 100 mM (concentration in the final reaction mixture) (D), rods are produced in greater than 90% yield. After decreasing the concentration of CTAB by 50%, (to 50 mM), average rod length decreased from 47 ± 5 to 39 ± 4 nm (C). Using 25 mM CTAB, nanorod products were of similar length, however, the yield of nanorods compared to pseudo-spherical products was reduced (from 95 to 71%).

3.5.2 Increasing Reagent Concentration Relative to Surfactant Concentration

Instead of directly reducing the surfactant concentration in the seedless syntheses (and thereby influence the supramolecular architecture of the surfactant), a more efficient approach to reducing the amount of CTAB was to increase the concentration of all reagents relative to CTAB. Here, reagent concentrations were increased between 3 and 15 times the concentrations used in our original seedless synthesis, while the concentration of CTAB was held constant at 200 mM and 50 mM for nanorods and nanoprisms, respectively. Here, the concentration of surfactant is maintained, yet the amount of surfactant required per nanoparticle product can be reduced, enabling total reductions in the surfactant concentration and cost upwards of 80%.

3.5.2.1 CTAB Efficient Synthesis of Nanorods

In CTAB efficient syntheses of seedless nanorods, increasing the reagent concentration by **5x** relative to that of CTAB led to the formation of nanorods in comparable yield and monodisperisty as those produced under standard reaction concentrations (Figure 3.10). The resulting particle products were produced at approximately five times the concentration, as indicated by extinction measurements (extinction at 750 nm increased 4.65 times compared to spectra taken of as-synthesized solutions produced in the standard synthesis). Increasing concentrations to **10x** leads to a population of cuboidal impurities, evident in the extinction spectra by increased absorbance at 535 nm (Figure 3.10 A, D).[64] At concentrations exceeding **10x**, nanorods decrease in aspect ratios as well as yield, as indicated by the decreasing intensity and blue-shift of the longitudinal LSPR to 612 nm (Figure 3.10 A).

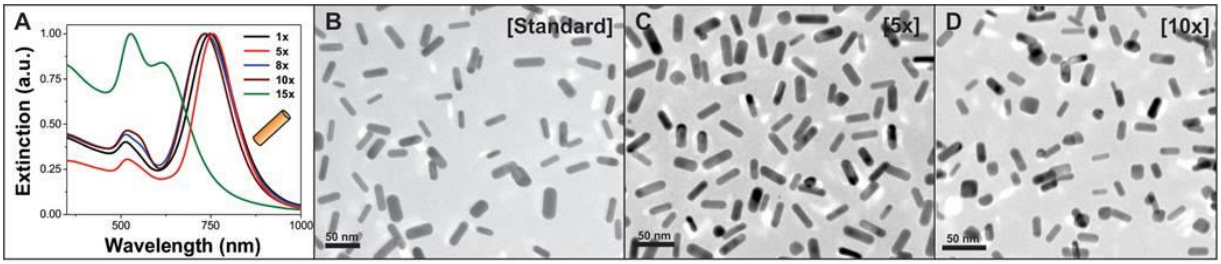

Figure 3.10. UV-vis-NIR spectra (A) and corresponding TEM images of nanorods produced using a CTAB-efficient, seedless approach (B-D). Upon increasing the reagent concentration with respect to CTAB concentration used in standard seedless conditions (B), no observable changes in product yield, monodisperisty, or morphology were observed even at a five-fold increase, **5x** (C). At concentrations greater than **5x**, the formation of pseudo-spherical and cuboidal particles begins to become competitive with rod growth (D).

3.5.2.2 CTAB Efficient Synthesis of Nanorprisms

Upon increasing the concentration of all reagents relative to CTAB in the seedless synthesis of gold nanoprisms, large changes in prism size and shape were observed (Figure 3.101. At **5x** concentration, the triangular prism shape was maintained, however edge lengths increased from 186 ± 16 nm to 217 ± 18 nm and thickness increased from 9 ± 1 nm to 25 ± 2 nm. When the reagent concentration was increased to **8x**, plate-like growth was still observed in similar yield (~60%), however, prism thickness again increased slightly (28 ± 3 nm) and particles adopted hexagonal geometries. Further, vertex-to-vertex distance decreased from 217 ± 18 nm to 125 ± 18 nm. Combined, these morphology changes led to a blue-shift of the dipole LSPR band (>250nm), which can be attributed to both "snipping" of the prism edges[65] as well as an increase in particle thickness[66]. Here, the changes in product morphology are consistent with previously proposed growth mechanisms based upon the Terrace-Step-Kink model. The presence of a twin plane defect on the side facets of nanoprisms results in a type of kink site, promoting a faster rate of Au incorporation on the sides of the prisms as compared to the top faces. At high concentrations of metal monomer, deposition on the top face competes effectively with deposition on the side facets, causing observable growth in both particle dimensions.

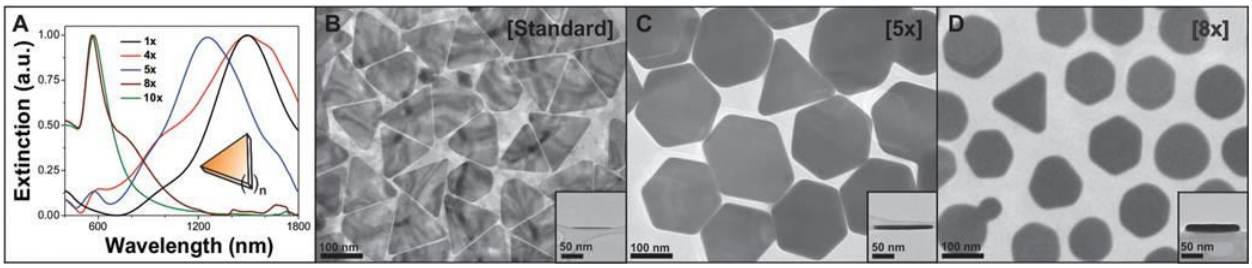

Figure 3.11. UV-vis-NIR spectra (A) and corresponding TEM images of nanoprisms produced using a CTAB-efficient, seedless approach (B-D). Using standard seedless conditions, nanoprisms exhibit characteristic optical features (in-plane dipole LSPR = 1510 nm) with average edge lengths of 143 ± 16 nm and average thickness of 9 ± 1 nm (B and inset). Prisms synthesized at **5x** displayed hexagonal morphologies with slightly longer vertex-to-vertex distances (217 ± 18 nm) and thickness of 25 ± 2 nm as well as a blue-shifted λ_{max} (1245 nm) (C and inset). At **8x** reagent concentrations, plate-like growth is still observed, but particles are smaller (vertex-to-vertex = 125 ± 18 nm) and thicker (28 ± 3 nm, D and inset).

3.6 Seedless Synthesis as a Sustainable Alternative to Seed-Mediated Growth Processes

Considering the effects of the $NaBH_4$:$HAuCl_4$ ratio and efficient CTAB usage conditions, optimized conditions (maximized yield of reaction products which are indistinguishable from those obtained using seed-mediated methods) were found to be **5x** and **3x** for nanorods and nanoprisms, respectively (Figure 3.12). Extinction spectra taken of dilute nanoparticle products (Figure 3.12 C,D) indicate that these particles exhibit characteristic spectral features, yet are produced in 3-5 times the concentration compared to literature protocols.

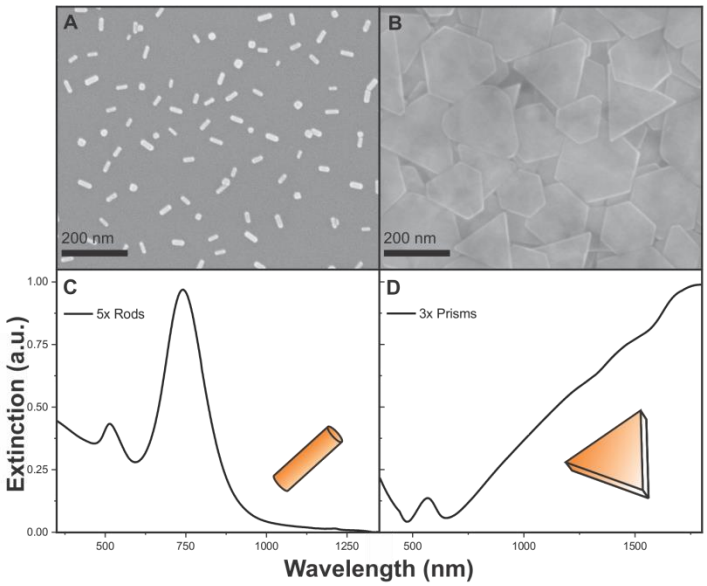

Figure 3.12. SEM images (A, B) and extinction spectra (C,D) of nanorods and nanoprisms, synthesized at **5x** and **3x**, respectively. Nanorods were 39 ± 6 nm in length, and nanoprisms had an average edge length of 183 ± 20 nm and average thickness of 21 ± 4 nm. These data demonstrate that characteristic morphologies and optical properties are observed from both shapes using CTAB-efficient, seedless initiation reaction conditions.

Efficient use of CTAB is crucial for the sustainability of nanoparticle syntheses, both in terms of atom economy and waste prevention. Optimization of seedless initiation conditions afforded reductions in the amount and total cost of CTAB by 80% and 66% for nanorods and nanoprisms, respectively These improvements, coupled with the elimination of seeds and extraneous reagents, allowed for a 91% and 88% decrease in the amount of reagents (by weight) necessary for the production of nanorods and nanoprisms, respectively (Figure 3.13).

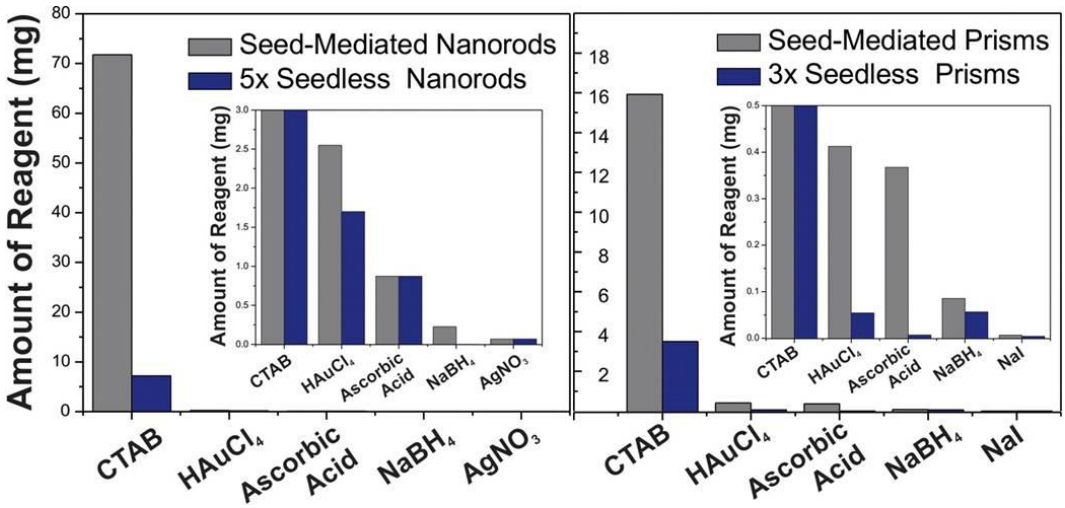

Figure 3.13. Comparison between the amount of reagents required for seed-mediated vs. seedless syntheses of gold nanorods (left) and gold nanoprisms (right). The total amount of reagent used is dominated by CTAB (as is the total cost, see SI). In total, the weight of reagents was reduced by 91% and 88% in the seedless CTAB-efficient synthesis of nanorods and nanoprisms, respectively, relative to the seed-mediated protocols. (Inset is a zoom-in of each bar graph to allow visualization of other reagents).

3.6.1 Approach to Evaluating Synthetic Efficiency

In comparing the efficiency of seeded and seedless methods, a value referred to as the amount of reagent per standard mL of nanoparticles was used as a qualitative relation between reagent weight and nanoparticle product yield for seeded and seedless syntheses. Here, the amount of reagent per standard mL of nanoparticles is the amount of reagents (in milligrams) required to synthesize 1 mL of nanoparticles at the concentration produced in a standard seed-mediated synthesis as determined by the optical density at at λ_{max}. These calculations are based on estimates of concentration using the optical density of nanoparticle solutions as every nanoparticle has a unique extinction coefficient based on its size, shape,

and composition. Here, the relationship between solution optical density and particle concentration is challenging to present quantitatively due to particle size and shape distributions which can vary from synthesis to synthesis. Instead, comparisons of concentration are relative rather than quantitative and are not converted to molarity.

For example, in a standard, seeded synthesis of nanorods[26] a total of 72.1 mg of reagents are used to produce 10.16 mL of nanorods. Therefore, 7.097 mg of reagents produce 1 mL of as-synthesized nanorods in this seed-mediated synthesis. Using our seedless method, 36.13 mg of reagents is used to produce 10.16 mL of nanorods at **1x**. Therefore 3.556 mg of reagents produce 1 mL of nanorods using a seedless approach. Here, optical density at the longitudinal LSPR is used to assess concentration. In both the seeded and seedless cases, the as-synthesized nanoparticle mixtures have similar optical density at the longitudinal LSPR peak maximum (OD = 0.62 at 706 nm, OD = 0.72 at 745 nm for seeded and seedless nanorods, respectively). For a comprehensive list of reagent quantities in the literature protocols for seedless and seeded syntheses, please refer to Table 3.1.

Synthesis	$HAuCl_4$ (mg)	CTAB (mg)	Ascorbic Acid (mg)	$NaBH_4$ (mg)	$AgNO_3$ (mg)	NaI (mg)	Trisodium Citrate (mg)
Nanorods (seeded)	2.55	729	0.872	0.227	0.0679	--	--
Nanorods (seedless)	1.70	364	0.872	0.0009	0.0679	--	--
Nanorods (seedless, **5x**)	8.49	364	4.36	0.00428	0.340	--	--
Nanoprisms (seeded)	4.25	164	0.881	3.78	--	0.0675	2.94
Nanoprisms (seedless)	0.941	182	0.977	0.117	--	0.0749	--
Nanoprisms (seedless, **3x**)	2.82	182	2.99	0.351	--	0.203	--

Table 3.1. Reagent quantities for seeded and seedless syntheses.

The following flow-chart summarizes the series of calculations used to determine the final amount of reagent per standard mL of nanoparticles for nanorods (Figure 3.14) and nanoprisms (Figure 3.15). Starting from the standard seed-mediated and seedless reagent experimental protocols, the amounts of each reagent required for the seed-mediated and seedless syntheses were plotted (top left). Next, these values were divided by the total reaction volume (**1**) to reach the concentration of reagents needed in the seed-mediated and seedless synthesis (in mg/mL). The seedless synthesis values were adjusted to reflect the amounts used in the CTAB efficient syntheses. For example, in the **5x** seedless nanorod synthesis, the concentrations of $HAuCl_4$, ascorbic acid, $NaBH_4$, and $AgNO_3$ were increased by a factor of 5 (**2**). Lastly, all values for the seedless syntheses were adjusted to reflect the total concentration of reagents needed to produce 1 mL of nanoparticles at concentrations produced in a standard seed-mediated synthesis and these are the values used to construct Figure 8 in the main text. Here, for instance, the reagent concentration values for the

seedless **5x** nanorods synthesis were divided by five to account for the increased nanorod yield per unit volume relative to the seed-mediated synthesis (**3**).

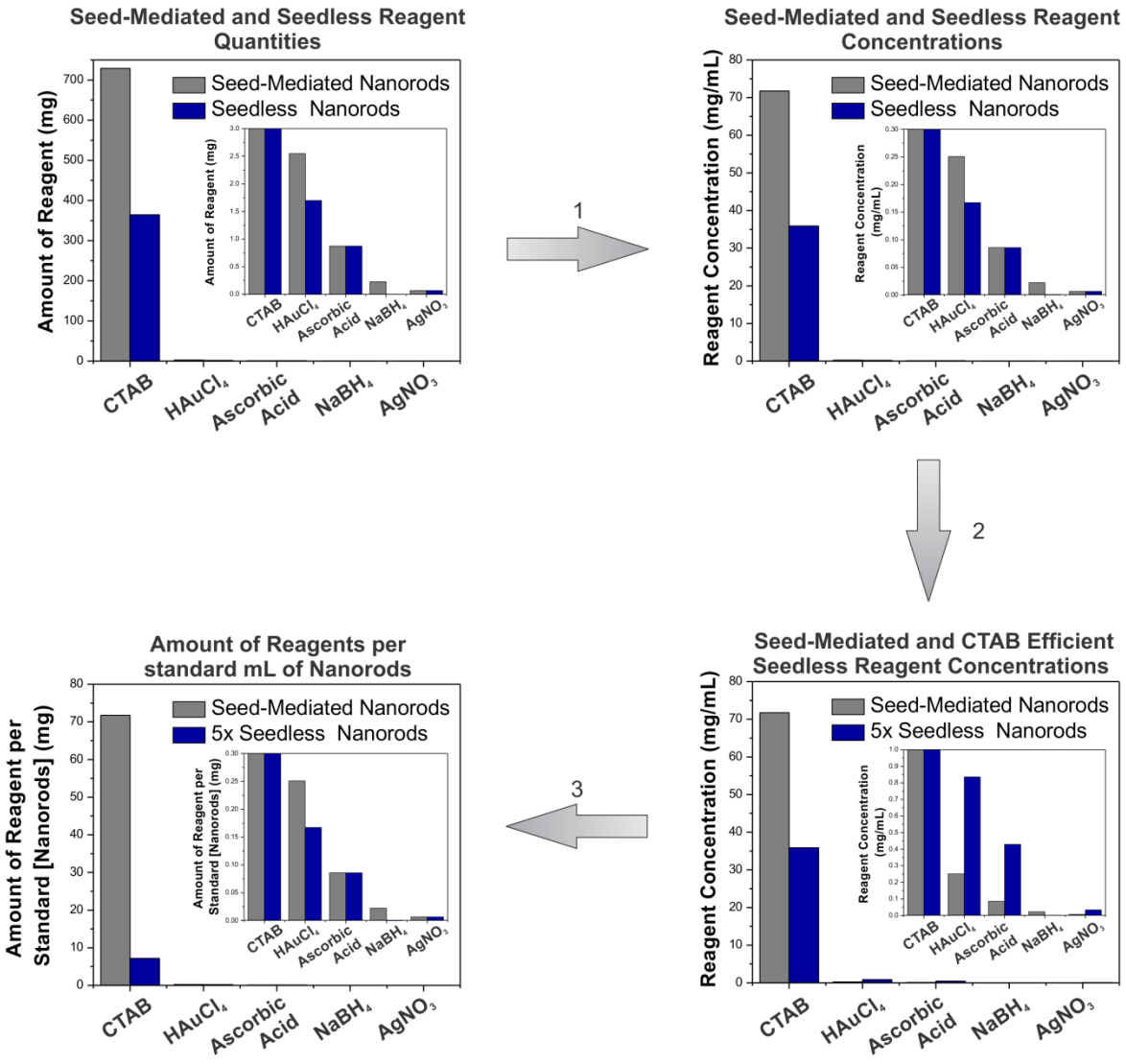

Figure 3.14. Flow-chart depicting the process used to determine the amount of reagents consumed in preparing a standard mL of nanorods using seed-mediated and seedless methods. Graph insets are a zoom-in of reagents that are used in much lower quantities than CTAB.

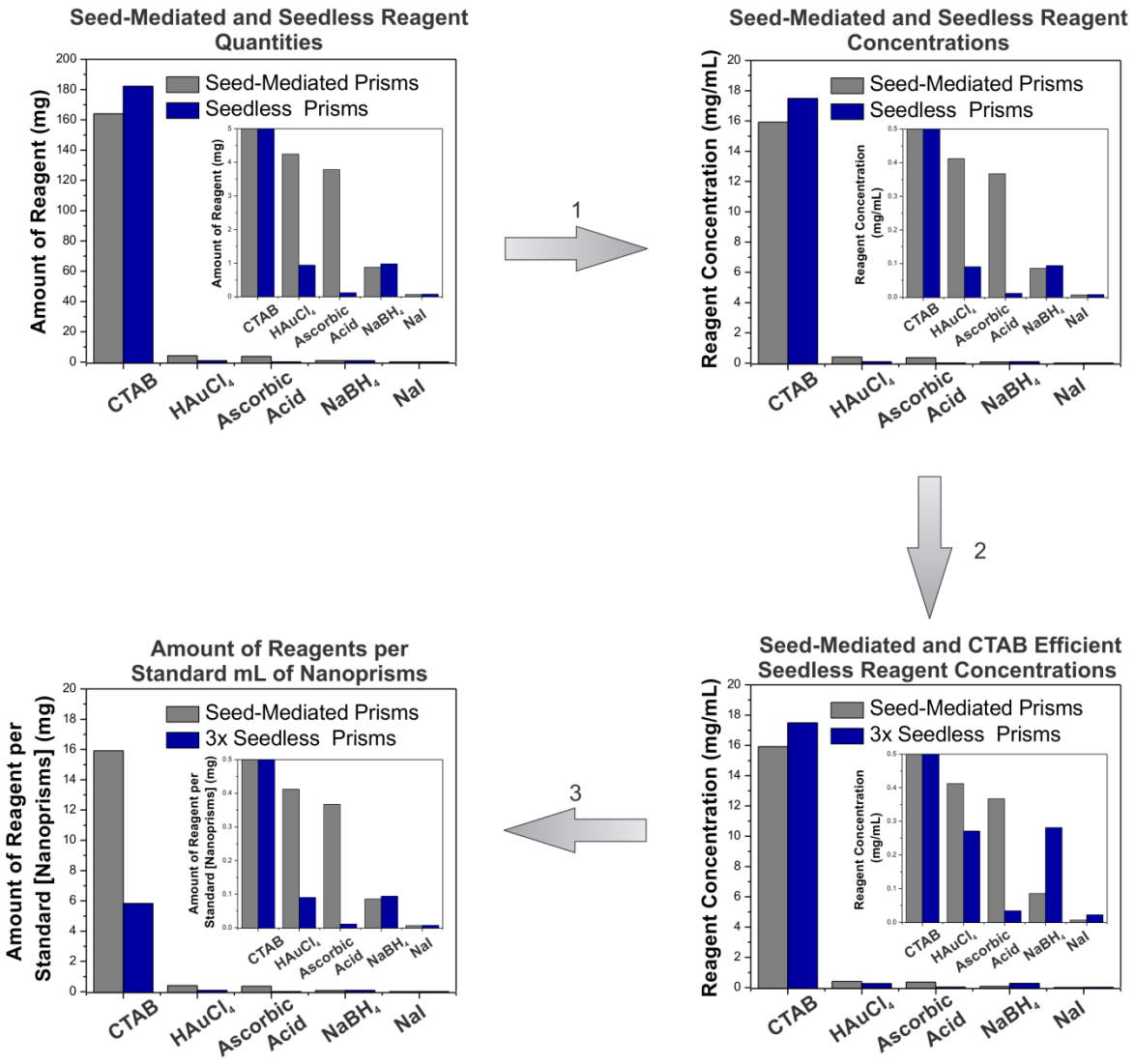

Figure 3.15. Flow-chart depicting the process used to determine the amount of reagents consumed in preparing a standard mL of nanoprisms using seed-mediated and seedless methods. Graph insets are a zoom-in of reagents that are used in much lower quantities than CTAB.

3.6.2 Approach to Evaluating Synthetic Cost

As a final means of comparing synthetic efficiency, the total amount of reagents per standard mL of nanoparticles was converted from reagent molecular weight to reagent cost.

Here, the conversion from reagent weight to reagent cost was performed in order to normalize differences in reagent cost and reagent amount. For instance, only 1.7 mg of $HAuCl_4$ are required for the synthesis of seedless gold nanorods, compared to 364 mg of CTAB. As $HAuCl_4$ is over 50 times more expensive that CTAB (Table 3.2), however, calculating reagent cost eliminates differences between quantity and price and allows for an accurate representation of the economic improvements afforded by seedless syntheses. As indicated in Figure 3.16, the total cost per standard mL of nanoparticles for seedless nanorods and nanoprisms has been reduced by 81% and 72%, respectively as compared to the seed-mediated protocols.

Reagent	Product Code (Sigma Aldrich)	Cost ($/g)
$HAuCl_4$	254169	196.60
$NaBH_4$	480886	3.97
$AgNO_3$	209139	3.88
CTAB	H9151	3.84
Ascorbic Acid	A7506	1.32
NaOH	306576	1.20
Trisodium Citrate	S4641	0.90
NaI	383112	0.68

Table 3.2. Reagent cost per gram.

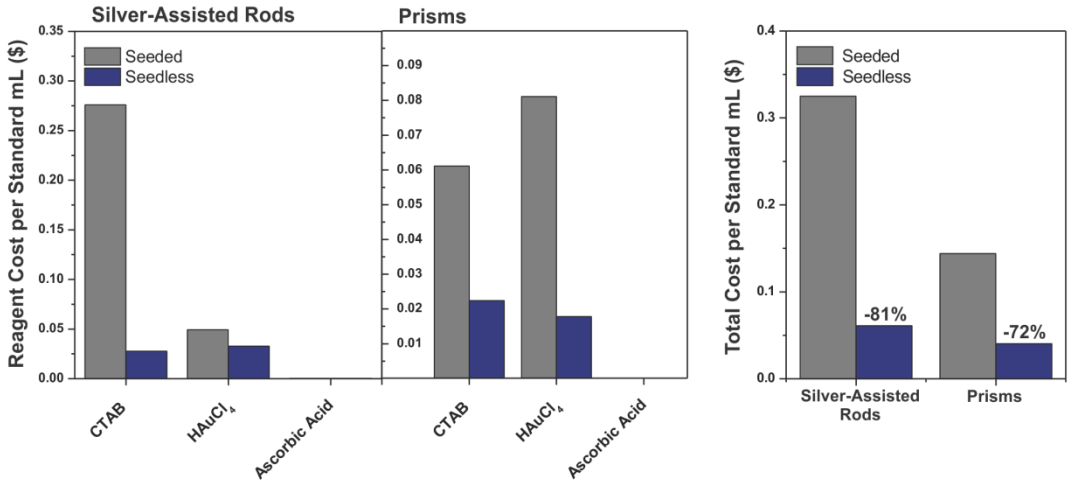

Figure 3.16. Total cost reductions in the three most expensive reagents (CTAB, $HAuCl_4$, and ascorbic acid) in seedless silver-assisted gold nanorods and gold nanoprisms, and total reduction in cost per standard mL of seeded and seedless syntheses.

4.0 CONCLUSIONS AND FUTURE DIRECTIONS

4.1 Conclusions

In conclusion, a homogeneous nucleation approach to canonical anisotropic gold nanoparticles has been developed. In developing the seedless methodology, the range of synthetically accessible nanoparticle product morphologies has been extended, allowing for increased tenability of the resulting optical, electronic, and catalytic properties. Elimination of the seed and extraneous regents also allows for sustainable reaction conditions, as nanoprisms and nanorods have been formed with almost identical crystallographic properties using up to 90% less reagent. These results shed new light on the fundamental mechanisms leading to anisotropic gold nanoparticle growth, and should accelerate the discovery and commercialization of applications based on anisotropic noble metal nanoparticles.

4.2 Future Directions

Having developed methods to produce pure, anisotropic nanomaterials in high yield, these materials will be investigated as substrates for the rational design of complex of complex hybrid nanoparticle architectures. Such hybrid architectures have shown orders of magnitude improvement in electronic and catalytic properties over their individual constituents[2, 67], and are therefore of immediate technological interest. In this approach, the anisotropic crystalline architecture allows for shape-controlled design of hybrid architectures, as the difference in crystal facet energetics can be used as a handle for reaction selectivity.

Our preliminary work in this area has concerned the site-selective deposition of platinum on the surface of gold nanoprisms. Here, underpotential deposition of platinum proceeds by

a Volmer-Weber mechanism[68], leading to the formation of Pt islands on the gold surface[69, 70] (Figure 4.1). Although the exact mechanism behind the deposition process is still under investigation, the regular arrangement of defect sites on the gold nanoprism cause the Pt islands to be deposited in uniform rows across the surface (Figure 4.2). Future work on this area will concern investigating the catalytic activity of the Pt clusters, as well as using the Pt as a shape directing functionality for the deposition of semiconducting materials[71].

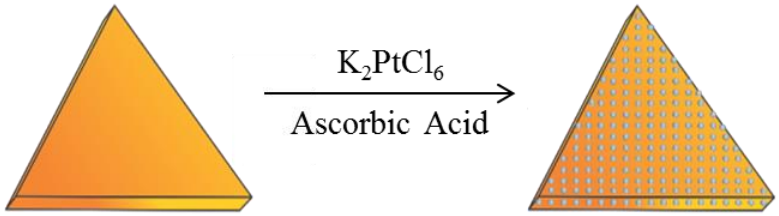

Figure 4.1. Reaction scheme for the underpotential deposition of Pt island rows on the surface of an Au nanoprism

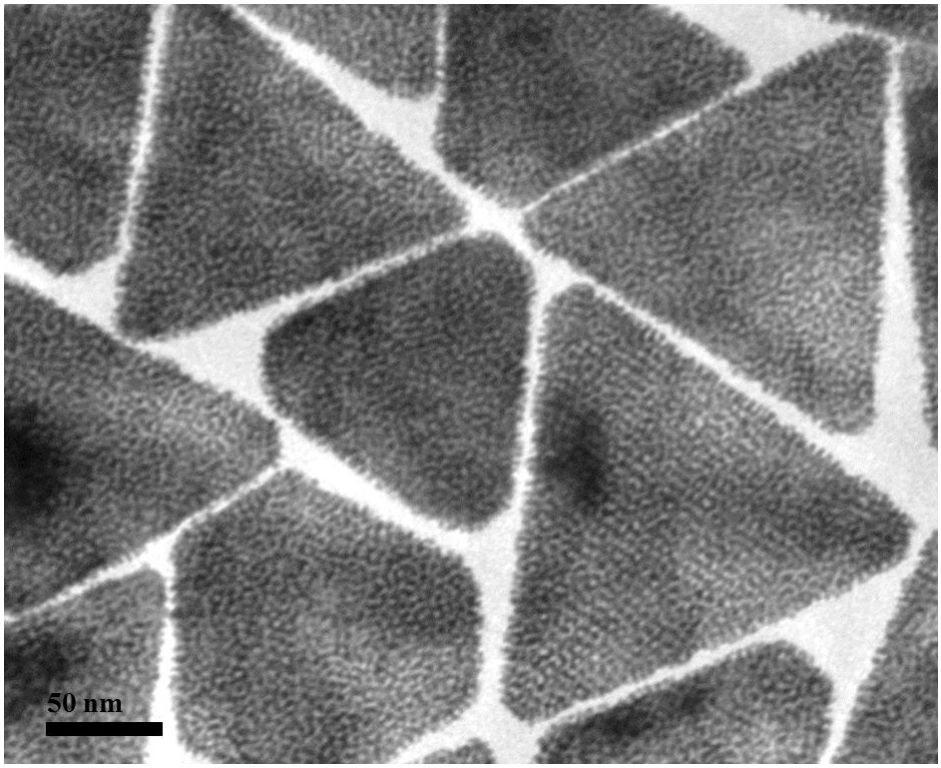

Figure 4.2. As indicated by TEM, the Pt islands are 3.9 ± 0.5 nm in diameter, arranged in rows separated by 5.9 ± 0.6 nm, where the separation distance is the center-to-center distance of Pt islands in adjacent rows.

REFERENCES

1. Jain, P. K.; Huang, X. H.; El-Sayed, I. H.; El-Sayed, M. A. Noble Metals on the Nanoscale: Optical and Photothermal Properties and Some Applications in Imaging, Sensing, Biology, and Medicine. *Accounts Chem. Res.* **2008,** *41*, 1578-1586.
2. Linic, S.; Christopher, P.; Ingram, D. B. Plasmonic-Metal Nanostructures for Efficient Conversion of Solar to Chemical Energy. *Nat. Mater.* **2011,** *10*, 911-921.
3. Luk'yanchuk, B.; Zheludev, N. I.; Maier, S. A.; Halas, N. J.; Nordlander, P.; Giessen, H.; Chong, C. T. The Fano Resonance in Plasmonic Nanostructures and Metamaterials. *Nat. Mater.* **2010,** *9*, 707-715.
4. Wiley, B.; Sun, Y.; Mayers, B.; Xia, Y. Shape-Controlled Synthesis of Metal Nanostructures: The Case of Silver. *Chem. Eur. J.* **2005,** *11*, 454-463.
5. Personick, M. L.; Langille, M. R.; Zhang, J.; Mirkin, C. A. Shape Control of Gold Nanoparticles by Silver Underpotential Deposition. *Nano Lett.* **2011,** *11*, 3394-3398.
6. Ahmadi, T. S.; Wang, Z. L.; Green, T. C.; Henglein, A.; El-Sayed, M. A. Shape-Controlled Synthesis of Colloidal Platinum Nanoparticles. *Science* **1996,** *272*, 1924-1925.
7. Jana, N. R.; Gearheart, L.; Murphy, C. J. Wet Chemical Synthesis of High Aspect Ratio Cylindrical Gold Nanorods. *J. Phys. Chem. B* **2001,** *105*, 4065-4067.
8. Salem, A. K.; Searson, P. C.; Leong, K. W. Multifunctional Nanorods for Gene Delivery. *Nat. Mater.* **2003,** *2*, 668-671.
9. Jones, M. R.; Millstone, J. E.; Giljohann, D. A.; Seferos, D. S.; Young, K. L.; Mirkin, C. A. Plasmonically Controlled Nucleic Acid Dehybridization with Gold Nanoprisms. *ChemPhysChem* **2009,** *10*, 1461-1465.
10. Lyons, P. E.; De, S.; Elias, J.; Schamel, M.; Philippe, L.; Bellew, A. T.; Boland, J. J.; Coleman, J. N. High-Performance Transparent Conductors from Networks of Gold Nanowires. *Phys. Chem. Lett.* **2011,** *2*, 3058-3062.
11. Hornyak, G.; Dutta, J.; Tibbals, H.; Rao, A., *Introduction to Nanoscience*. CRC Press: New York, 2008; p 815.
12. Tao, A. R.; Habas, S.; Yang, P. Shape Control of Colloidal Metal Nanocrystals. *Small* **2008,** *4*, 310-325.
13. LaMer, V. K.; Dinegar, R. H. Theory, Production and Mechanism of Formation of Monodispersed Hydrosols. *J. Am. Chem. Soc.* **1950,** *72*, 4847-4854.
14. Schmelzer, J., *Nucleation Theory and Applications*. Wiley: New York, 2005; p 455.
15. Shafrin, E. G.; Zisman, W. A. Constitutive Relations in the Wetting of Low Energy Surfaces and the Theory of the Retraction Method of Preparing Monolayers. *J. Phys. Chem.* **1960,** *64*, 519-524.
16. Kossel, W. Extenoling the Law of Bravais. *Nach Ges Wiss Gottingen* **1927**, 143.
17. Imai, Y.; Mukaida, M.; Watanabe, A. T., T. Formation Energies of Two-Dimensional Nuclei Randomly-Generated on (001), (110), and (111) Planes of a Face-Centered-Cubic Crystal. *Thin Solid Films* **1997,** *300*, 305-313.
18. Love, C. J.; Estroff, L. A.; Kriebel, J. K.; Nuzzo, R. G.; Whitesides, G. M. Self-Assembled Monolayers of Thiolates on Metals as a Form of Nanotechnology. *Chem. Rev.* **2005,** *105*, 1103-1169.
19. Lofton, C.; Sigmund, W. Mechanisms Controlling Crystal Habits of Gold and Silver Colloids. *Adv. Funct. Mater.* **2005,** *15*, 1197-1208.

20. Larsen, K.; Bechgaard, K.; Stipp, S. L. S. The effect of the Ca2+ to activity ratio on spiral growth at the calcite surface. *Geochimica et Cosmochimica Acta* **2010,** *74*, 2099-2109.
21. Turkevich, J.; Stevenson, P. C.; Hillier, J. A Study of the Nulceation and Growth Processes in the Synthesis of Colloidal Gold. *Discuss. Faraday Soc.* **1951,** *11*, 55-75.
22. Brown, K. R.; Walter, D. G.; Natan, M. J. Seeding of Colloidal Au Nanoparticle Solutions. 2. Improved Control of Particle Size and Shape. *Chem. Mater.* **2000,** *12*, 306-313.
23. Wiley, B.; Herricks, T.; Sun, Y.; Xia, Y. Polyol Synthesis of Silver Nanoparticles: Use of Chloride and Oxygen to Promote the Formation of Single-Crystal, Truncated Cubes and Tetrahedrons. *Nano Lett.* **2004,** *4*, 1733-1739.
24. Liu; Guyot-Sionnest, P. Mechanism of Silver(I)-Assisted Growth of Gold Nanorods and Bipyramids. *J. Phys. Chem. B* **2005,** *109*, 22192-22200.
25. Millstone, J. E.; Wie, W.; Jones, M. R.; Yoo, H.; Mirkin, C. A. Iodide Ions Control Seed-mediated Growth of Anisotropic Gold Nanoparticles. *Nano Lett.* **2008,** *8*, 2526-2529.
26. Nikoobakht, B.; El-Sayed, M. A. Preparation and Growth Mechanism of Gold Nanorods (NRs) Using Seed-Mediated Growth Method. *Chem. Mater.* **2003,** *15*, 1957-1962.
27. Millstone, J. E.; Park, S.; Shuford, K. L.; Qin, L.; Schatz, G. C.; Mirkin, C. A. Observation of a Quadrupole Plasmon Mode for a Colloidal Solution of Gold Nanoprisms. *J. Am. Chem. Soc.* **2005,** *127*, 5312-5313.
28. Langille, M. R.; Personick, M. L.; Zhang, J.; Mirkin, C. A. Defining Rules for the Shape Evolution of Gold Nanoparticles. *J. Am. Chem. Soc.* **2012,** *134*, 14542-14554.
29. Orendorff, C. J.; Murphy, C. J. Quantitation of Metal Content in the Silver-Assisted Growth of Gold Nanorods. *J. Phys. Chem. B* **2006,** *110*, 3990-3994.
30. Schmuki, P.; SVirtanen, S., *Electrochemistry at the Nanoscale*. Springer: Erlangen, Germany, 2009; p 471.
31. Mrozek, P.; Sung, Y. E.; Wieckowski, A. Silver Deposition on the Au(111) Electrode without Interference by Specifically Adsorbed Anions. *Surf. Sci.* **1995,** *335*, 44-51.
32. Seo, D.; Park, J. H.; Jung, J.; Park, S. M.; Ryu, S.; Kwak, J.; Song, H. One-Dimensional Gold Nanostructures through Directed Anisotropic Overgrowth from Gold Decahedrons. *J. Phys. Chem. C* **2009,** *113*, 3449-3454.
33. Hakkinen, H.; Merikoski, J.; Manninen, M. Surface Reconstruction and Many-Atom Models. *J. Phys. Condens. Mat.* **1991,** *3*, 2755-2767.
34. Elechiguerra, J. L.; Reyes-Gasga, J.; Yacaman, M. J. The Role of Twinning in Shape Evolution of Anisotropic Noble Metal Nanostructures. *J. Mater. Chem.* **2006,** *16*, 3906-3919.
35. Shuford, K. L.; Ratner, M. A.; Schatz, G. C. Multipolar Excitation in Triangular Nanoprisms. *J. Chem. Phys.* **2005,** *123*, 1147131-9.
36. Jain, P. K.; Lee, K. S.; El-Sayed, I. H.; El-Sayed, M. A. Calculated Absorption and Scattering Properties of Gold Nanoparticles of Differenct Size, Shape, and Composition: Applications in Biological Imaging and Biomedicine. *J. Phys. Chem. B* **2006,** *110*, 7238-7248.
37. Hollamby, M. J.; Eastoe, J.; Chemelli, A.; Glatter, O.; Rogers, S.; Heenan, R. K.; Grillo, I. Separation and Purification of Nanoparticles in a Single Step. *Langmuir* **2009,** *26*, 6989-6994.
38. Zhu, M.; Lanni, E.; Garg, N.; Bier, M. E.; Jin, R. Kinetically Controlled, High-Yield Synthesis of Au_{25} Clusters. *J. Am. Chem. Soc.* **2008,** *130*, 1138-1139.
39. Personick, M. L.; Langille, M. R.; Zhang, J.; Harris, N.; Schatz, G. C.; Mirkin, C. A. Synthesis and Isolation of {110}-Faceted Gold Bipyramids and Rhombic Dodecahedra. *J. Am. Chem. Soc.* **2011,** *133*, 6170-6173.

40. Salabat, A.; Eastoe, J.; Mutch, K. J.; Tabor, R. F. Tuning Aggregation of Microemulsion Droplets and Silica Nanoparticles Using Solvent Mixtures. *J. Colloid Interf. Sci.* **2008,** *318*, 244-251.
41. Wei, G.; Liu, F. Separation of Nanometer Gold Particles by Size Exclusion Chromatography. *J Chromatogr.* **1999,** *836*, 253-260.
42. Engel, T.; Reid, P., *Physical Chemistry*. Pearson: San Francisco, 2006; p 1061.
43. Willets, K. A.; Van Duyne, R. P. Localized Surface Plasmon Resonance Spectroscopy and Sensing. *Annu. Rev. Phys. Chem.* **2007,** *58*, 267-297.
44. Brockman, J. M.; Nelson, B. P.; Corn, R. M. Surface Plasmon Resonance Imaging Measurments of Ultrathin Organic Films. *Ann. Rev. Phys. Chem.* **2000,** *51*, 41-63.
45. Skoog, D. A.; Holler, F. J.; Nieman, T. A., *Principles of Instrumental Analysis* 5th ed.; Harcourt Brace: Orlando, 1998; p 849.
46. Eustis, S.; El-Sayed, M. A. Why gold nanoparticles are more precious than pretty gold: Noble metal surface plasmon resonance and its enhancement of the radiative and nonradiative properties of nanocrystals of different shapes. *Chemical Society Reviews* **2006,** *35*, 209-217.
47. Erni, R.; Rossell, M. D.; Kisielowski, C.; Dahmen, U. Atomic-Resolution Imaging with a Sub-50-pm Electron Probe. *Phys. Rev. Lett.* **2009,** *102*, 096101.
48. Ruska, E. The Early Development of Electron Lenses and Electron Microscopy. *Microsc. Acta. Suppl.* **1980,** *5*, 1-140.
49. Nixon, W. C. The General Principles of Scanning Electron Microscopy. *Philos. T. Roy. Soc. B* **1971,** *261*, 45-50.
50. Dahl, J. A.; Maddux, L. S.; Hutchison, J. E. Toward Greener Nanosynthesis. *Chem. Rev.* **2007,** *107*, 2228-2269.
51. Anastas, P.; Warner, J., *Green Chemistry: Theory and Practice*. Oxford University Press: New York, 1998.
52. Goyal, P. S.; Dasannacharya, B. A.; Kelkar, V. K.; Manohar, C.; Srinivasa Rao, K.; Valaulikar, B. S. Shapes and Sizes of Micelles in CTAB Solutions. *Physica B* **1991,** *174*, 196-199.
53. Imae, T.; Kamiya, R.; Ikeda, S. Formation of Spherical and Rod-Like Micelles of Cetyltrimethylammonium Bromide in Aqueous NaBr. *J. Colloid Interf. Sci.* **1985,** *108*, 215-225.
54. Gao, J.; Bender, C. M.; Murphy, C. J. Dependence of the Gold Nanorod Aspect Ratio on the Nature of the Directing Surfactant in Aqueous Solution. *Langmuir* **2003,** *19*, 9065-9070.
55. Rodriguez-Fernandez, J.; Perez-Juste, J.; Mulvaney, P.; Liz-Marzan, L. M. Spatially-Directed Oxidation of Gold Nanoparticles by Au(III)-CTAB Complexes. *Phys. Chem. Lett. B* **2005,** *109*, 14257-14261.
56. Uppal, M. A.; Kafizas, A.; Lim, T. H.; Parkin, I. P. The Extended Time Evolution Size Decrease of Gold Nanoparticles Formed by the Turkevich Method. *New. J. Chem.* **2010,** *34*, 1401-1407.
57. Lide, D., *CRC Handbook of Chemistry and Physics, 88th Edition (CRC Handbook of Chemistry & Physics)*. CRC Press: 2007.
58. Chatenet, M.; Micoud, F.; Roche, I.; Chainet, E. Kinetics of Sodium Borohydride Direct Oxidation and Reduction in Sodium Hydroxide Electrolyte: Part 1. BH_4^- Electrooxidation on Au and Ag Catalysts. *Electrochim. Acta* **2006,** *51*, 5459-5467.
59. Millstone, J. E.; Hurst, S. J.; Metraux, G. S.; Cutler, J. I.; Mirkin, C. A. Colloidal Gold and Silver Triangular Nanoprisms. *Small* **2009,** *5*, 646-664.

60. Hubert, F.; Testard, F.; Rizza, G.; Spalla, O. Nanorods versus Nanospheres: A Bifurcation Mechanism Revealed by Principal Component TEM Analysis. *Langmuir* **2010,** *26*, 6887-6891.
61. Edgar, J. A.; McDonagh, A. M.; Cortie, M. B. Formation of Gold Nanorods by a Stochastic "Popcorn" Mechanism *ACS Nano* **2012,** *6*, 1116.
62. Katz-Boon, H.; Rossouw, C. J.; Weyland, M.; Funston, A. M.; Mulvaney, P.; Etheridge, J. Three-Dimensional Morphology and Crystallography of Gold Nanorods. *Nano Lett.* **2010,** *11*, 273-278.
63. Alkilany, A. M.; Nagaria, P. K.; Hexel, C. R.; Shaw, T. J.; Murphy, C. J.; Wyatt, M. D. Cellular Uptake and Cytotoxicity of Gold Nanorods: Molecular Origin of Cytotoxicity and Surface Effects. *Small* **2009,** *5*, 701-708.
64. Wu, H.; Kuo, C.; Huang, M. H. Seed-Mediated Synthesis of Gold Nanocrystals with Systematic Shape Evolution from Cubic to Trisoctahedral and Rhombic Dodecahedral Structures. *Langmuir* **2010,** *26*, 12307-12313.
65. Kelly, K. L.; Coronado, E.; Zhao, L. L.; Schatz, G. C. The Optical Properties of Metal Nanoparticles: The Influence of Size, Shape, and Dielectric Environment. *J. Phys. Chem. B* **2003,** *107*, 668-677.
66. Metraux, G. S.; Mirkin, C. A. Nanoprisms with Chemically Tailorable Thickness. *Adv. Mater.* **2005,** *17*, 412-415.
67. Sheldon, M. T.; Trudeau, P.; Mokari, T.; Wang, L.; Alivisatos, A. P. Enhanced Semiconductor Nanocrystal Conductance via Solution Grown Contacts. *Nano Lett.* **2009,** *9*, 3676-3682.
68. Fan, F.-R.; Liu, D.-Y.; Wu, Y.-F.; Duan, S.; Xie, Z.-X.; Jiang, Z.-Y.; Tian, Z.-Q. Epitaxial Growth of Heterogeneous Metal Nanocrystals: From Gold Nano-octahedra to Palladium and Silver Nanocubes. *J. Am. Chem. Soc.* **2008,** *130*, 6949-6951.
69. Friesen, C.; Seel, S. C.; Thompson, C. V. Reversible Stress Changes at all Stages of Volmer--Weber Film Growth. *J. Appl. Phys.* **2004,** *95*, 1011-1020.
70. Grzelczak, M.; Perez-Juste, J.; Rodriguez-Gonzalez, B.; Liz-Marzan, L. M. Influence of Silver Ions on the Growth Mode of Platinum on Gold Nanorods. *J. Mater. Chem.* **2006,** *16*, 3946-3951.
71. Buck, M.; Bondi, J. F.; Schaak, R. E. A Total-Synthesis for the Construction of High-Order Colloidal Hybrid Nanoparticles. *Nat. Chem.* **2012,** *4*, 37-44.